

Abstract

Nowadays, High Voltage Direct Current (HVDC) systems based on Voltage Source Converters (VSC) are being installed for integrating the energy of individual offshore wind power plants to the main land AC grid. Moreover, as the number of offshore wind power plants is increasing, the interconnection of the different links in a multi-terminal grid, to increase the system flexibility, becomes interesting. In this work, the different elements of a multi-terminal VSC-HVDC grid are modelled, VSC converters controllers are designed and the complete system is simulated employing Matlab Simulink to analyse the operation in different scenarios.

Contents

Preface	9
1 Introduction	11
1.1 System under analysis and objectives	11
1.2 Project structure	13
2 System parts and modelling	15
2.1 Wind farm and wind farm converter modelling	15
2.2 HVDC line modelling	15
2.3 AC line modelling	16
2.4 Voltage source converter modelling and control	16
2.4.1 Voltage source converter modelling	16
2.4.2 Voltage source converter control	17
3 HVDC cable models	25
3.1 Pi model	25
3.2 Pi model with multiple sections	26
3.3 Pi coupled model	28
3.4 Bergeron line model	30
4 Control design	35
4.1 Justification of the type of controller used	35
4.2 Control design assumptions	35
4.3 Control problem definition	37

5	Controller frequency analysis	41
5.1	System parameters and droop calculation for steady state case	41
5.2	Methodology description	42
5.3	Pi model analysis	43
5.3.1	Stability analysis	43
5.3.2	Frequency analysis	44
5.4	Pi multi-section model analysis	46
5.4.1	Stability analysis	46
5.4.2	Frequency analysis	47
5.5	Pi coupled model analysis	50
5.5.1	Stability analysis	50
5.5.2	Frequency analysis	51
6	Simulation results	53
6.1	Temporal response of the DC droop controller in front of a stepwise current input	55
6.2	Simulation results for a power step input	56
	Conclusions	63
	Acknowledgements	65
A	Budget	67
A.1	Office supplies	67
A.1.1	Hardware	67
A.1.2	Software	67
A.2	Human resources	68
A.3	Total budget	68
B	Environmental impact assessment	69
B.1	Seabed impact	69
B.2	Marine ecosystem impact	69
B.3	Atmospheric effects	70
B.4	Impact in humans	70
C	Park transformation	71

Control and simulation of multi-terminal VSC-HVDC grids for offshore wind integration	5
D Distributed parameters model vs Bergeron line model	73
Bibliography	77

List of Figures

1.1	General scheme	12
1.2	Two terminals scheme	12
2.1	Wind farm and wind farm converter modelling	15
2.2	Voltage Source Converter scheme	17
2.3	Voltage source converter model	17
2.4	Voltage source converter control scheme	18
2.5	Droop control	19
2.6	Reference computation	19
2.7	Connexion between the AC side of the converter and the AC grid	20
2.8	Current loop decoupled model	21
2.9	Current loop implementation	22
2.10	Phase locked loop general scheme	22
3.1	Pi model representation	25
3.2	Three Pi model series representation	27
3.3	Scheme cable section	28
3.4	Coupled Pi model representation	29
3.5	Differential of cable	30
3.6	k,m notation	32
3.7	Norton equivalent for the Bergeron model implementation	33
3.8	Norton equivalent when a lossy line is considered	34
4.1	General scheme for the two terminals case	35
4.2	Simplification of the current loop at the AC grid side converter	36
4.3	Simplified model	36

4.4	Notation of simplified model	37
5.1	Stability analysis for 1 Pi section	44
5.2	Bode diagram for $S(s)G_{yw}(s)$	44
5.3	Bode diagram for $KS(s)G_{yw}(s)$	45
5.4	Converter Bode diagram	46
5.5	Stability analysis for 2 Pi sections	47
5.6	Stability analysis for 100 Pi sections	47
5.7	Bode diagram for $S(s)G_{yw}(s)$ (2 Pi sections)	48
5.8	Bode diagram for $KS(s)G_{yw}(s)$ (2 Pi sections)	48
5.9	Bode diagram for $S(s)G_{yw}(s)$ (10 Pi sections)	49
5.10	Bode diagram for $KS(s)G_{yw}(s)$ (10 Pi sections)	49
5.11	Bode diagram for $S(s)G_{yw}(s)$ (50 Pi sections)	50
5.12	Bode diagram for $KS(s)G_{yw}(s)$ (50 Pi sections)	50
5.13	Stability analysis for Pi coupled model	51
5.14	Bode diagram for $S(s)G_{yw}(s)$ (Pi coupled model)	51
5.15	Bode diagram for $KS(s)G_{yw}(s)$ (Pi coupled model)	52
6.1	System implementation using Matlab Simulink	53
6.2	Droop control and reference computation implementation	54
6.3	Current loop implementation	54
6.4	Reference computation implementation	55
6.5	Temporal response of the DC bus for each model considering a 875 A step	56
6.6	Temporal response of I_{DC} for the different cable models	57
6.7	Temporal response of the DC bus for each model considering the wind farm converter	58
6.8	Temporal response of I_{abc} considering one Pi section	59
6.9	Temporal response of I_{abc} considering ten Pi sections	60
6.10	Temporal response of I_{abc} considering the Pi coupled model	61
6.11	Temporal response of I_{abc} considering the Bergeron model	62
B.1	HVDC installation	70
C.1	Geometrical interpretation	71
D.1	Differential of cable	73

Preface

In the recent years, renewable energies have grown significantly in front to the conventional energy sources. An example of this is the wind power. Basically, this technology consists in obtaining the energy present in an air flow thanks to the wind turbines and transforming it into electrical power.

The emplacement of this wind turbines, that is, the wind farm park, normally is in a geographic place in where the wind conditions are optimal in aim to ensure a good performance. However, the location of this wind farms has changed in the recent years, leading to the so-known offshore wind farms.

Offshore wind farms have several advantages compared to the onshore ones. First of all, the visual impact is reduced if the plant is far enough from the coast. Secondly, logistic problems such as roads with sharp curves or with weight limitations are avoided offshore, so the wind turbines can be bigger and more powerful. Finally, an important advantage is that the wind conditions are much more optimal offshore, making the wind farms with more power capability than the onshore ones.

However, the offshore wind farm has to be connected to the AC grid in order to transfer the generated power. Assuming this connection to be submarine, the energy losses are bigger if the line uses alternating current due to the inductive and capacitive effects. For that reason, HVDC (High Voltage Direct Current) is the most suitable technology because this so-mentioned effects are inexistent during the steady state, making this technology the most economically profitable.

This work has been supported by the Spanish Ministry of Economy and Competitiveness under the project ENE2013-47296. This research was co-financed by the European Regional Development Fund (ERDF).

Chapter 1

Introduction

In this chapter the contents and objectives of this work are exposed. The system under analysis is explained qualitatively, and the project structure including a brief explanation of each chapter is detailed.

1.1 System under analysis and objectives

The system under analysis is an offshore wind farm plant connected to the AC onshore grid by a multi-terminal HVDC line. The connection is performed by means of HVDC links using as many VSC converters as the number of terminals. These type of converters are not only able to transform the current nature (from AC to DC), but also to regulate the active and reactive power flow. The system is sketched in Figure 1.1.

Each system part will be explained in more detail in Chapter 2. Regarding the objectives of the work, they mainly are:

- Modelling of a VSC converter using an averaged model and studying deeply all of its parts.
- Analysis of the different cable models in aim to determine its impact on the design of the grid voltage control.
- Design of the droop voltage control performed by the AC grid side converter.

Typically, the control used in this kind of systems is a proportional controller [5], widely know as droop control. It could be thought that other control typologies are also suitable, as for example the conventional PI controller that could be able to reach a zero steady state error more effectively. The problem arises when using a PI controller at each of these terminals, as the integral parts of the different controllers will interact with each other. This interaction could lead to establish a power sharing different from the required values.

This is avoided by using a proportional controller, making each controller independent to the others and simplifying the control design. Due to the proportional nature of the

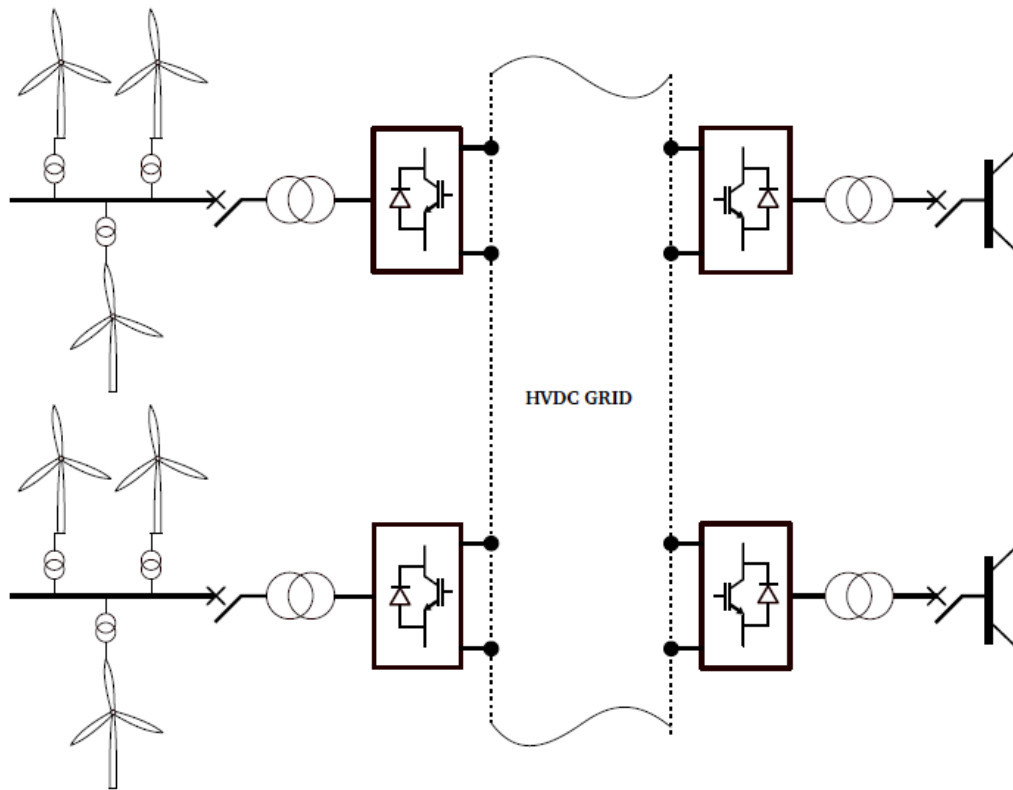


Figure 1.1: General scheme

controller, the steady state error will not be zero during the operation. However, it can be limited to a maximum value with an appropriate control design.

This project is focused on the impact of the cable model on the design of the multi-terminal droop control. In order to simplify the problem, the analysis is focused on a two terminal grid as shown in Figure 1.2, which allows to better understand the differences between the different cable models implemented. Furthermore, the procedure applied in the two-terminal case can be extrapolated to a multi-terminal case, so the conclusions extracted are valid in both cases.

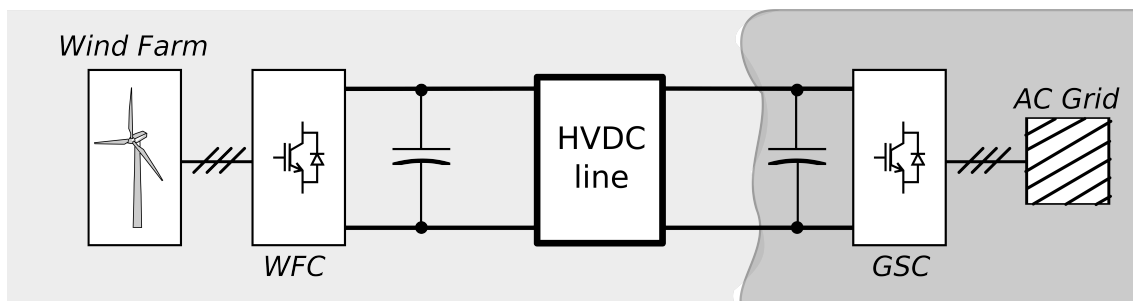


Figure 1.2: Two terminals scheme

1.2 Project structure

This work is structured in six chapters. In Chapter 2, as it is mentioned above, all the system parts are explained in detail. In this second chapter is in where the model used to represent the converter is explained, and also its implementation in Matlab.

In Chapter 3, the next cable models are analysed: the Pi model, the Pi model with multiple sections, the Pi coupled model, and the Bergeron model. For each model, its equations are explained and deduced and for the three first ones a space state notation is obtained in aim to be able to do a frequency analysis.

In Chapter 4, both the justification of the controller used and the control problem are explained.

Chapter 5 a frequency analysis is performed in the frequency domain to consider the transient state in the controller design. In this chapter a range of valid values for the K_{droop} is obtained.

Finally, in Chapter 6 a simulation using the value for K_{droop} found in Chapter 5 is done in aim to validate the results.

Chapter 2

System parts and modelling

As it is shown in Figure 1.1, the parts involved in the connexion between the wind farm and the AC grid are: the wind farm itself, the wind farm converter, the HVDC grid, the AC grid side converter (in which the control is applied), and the AC grid. In this chapter the modelling of each part is detailed.

2.1 Wind farm and wind farm converter modelling

The wind farm and the wind farm converter are modelled together by a controlled current source as it is shown in Figure 2.1 [5]. This current represents the output of the wind farm converter.

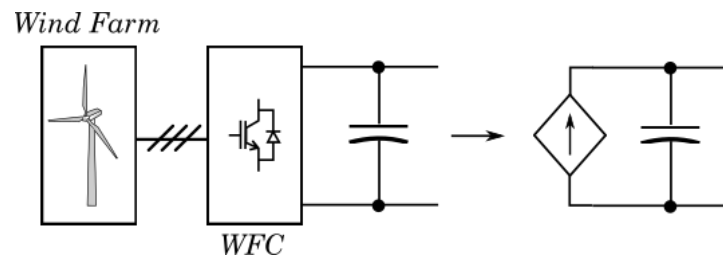


Figure 2.1: Wind farm and wind farm converter modelling

2.2 HVDC line modelling

Four different models of a HVDC line are studied in this work. These models are the Pi model, the Pi model with multiple sections, the Pi coupled model, and finally the Bergeron model. All of them are explained in more detail in Chapter 3. It is worth to understand these models as MIMO (Multiple Input Multiple Output) systems, in which the system inputs are the wind farm and the DC currents and the system outputs are the wind farm and the DC voltages. The corresponding modelling is explained in Chapter 4 in where the control design is also detailed.

It is worth to remind that a two terminal HVDC line is considered in order to simplify the control design, however, as said in Chapter 1 the results obtained can be extrapolated to multi-terminal cases.

2.3 AC line modelling

The AC line considered in this work is a high voltage three phase equilibrated line that is modelled by its Thévenin equivalent. The RMS phase-phase is 320 kV and its electric parameters are calculated taking [1] as reference and they are shown in the next table.

Parameter	Value	Units
S_{base}	526	MVA
V_{base}	320	kV
R_{pu}	0,01	pu
L_{pu}	0,15	pu

Table 2.1: AC line parameters

2.4 Voltage source converter modelling and control

The different converters connected to the HVDC grid are assumed to be equal. The wind farm model has already been described and, in this section, the modelling procedure for the grid side converter is detailed.

2.4.1 Voltage source converter modelling

The main function of the converter is to inject the energy that comes from the HVDC grid to the AC grid. To make this possible, the converter has to change the HVDC current nature in order to inject the incoming power to the AC grid. For offshore wind applications, specially for offshore HVDC transmission, VSC technology is preferred in comparison to Line Commutated Converter (LCC), due to several advantages as the independent control of active and reactive power, no commutation failure, black-start capability, reduced footprint, lighter cables and also there is no need for reverse polarity to reverse power [5]. Specifically, the main VSC converter topology employed in this application is the Modular Multilevel Converters (MMC).

This converter is compounded by different cells or sub-modules, that can switch between two different voltage states. The most common cell topology is based on a half bridge structure using IGBTs. A three-phase MMC is typically based by a large number of sub-modules per arm, and two different arms compound a phase unit. Figure 2.2 shows a picture of a phase unit of the converter.

This converter is able to apply an AC sinusoidal voltage based on the connection and disconnection of the different sub-module, by means of the modulation. In this work, in

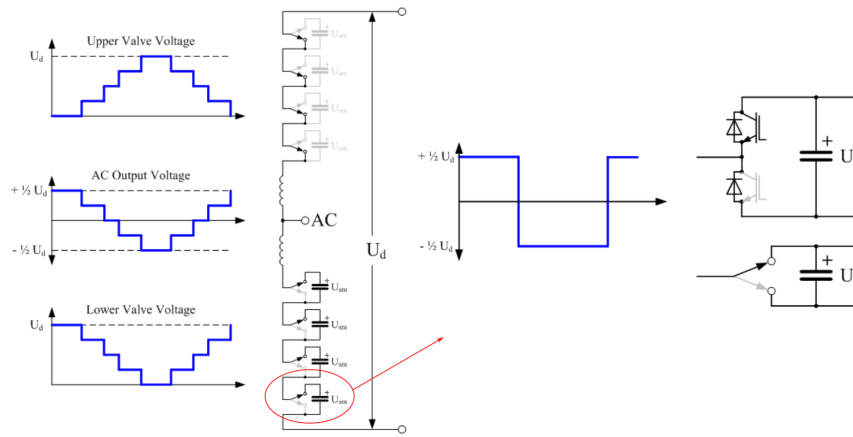


Figure 2.2: Voltage Source Converter scheme

order to simulate the behaviour of the converter it is used the so-known averaged model [2]. This model consists in decoupling the AC and the DC part of the converter as shown in Figure 2.3.

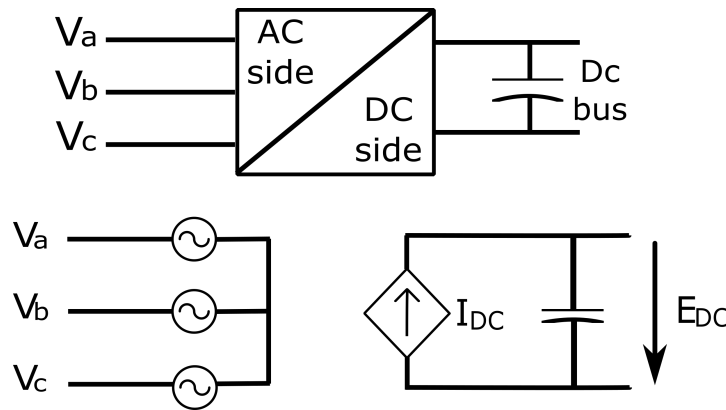


Figure 2.3: Voltage source converter model

With this technique, the necessary AC voltage is assumed to be applied by three controlled voltage sources. Note that with this model the switching losses are not considered. The relation between the AC and the DC part is obtained by a balance of active power (2.1).

$$I_{DC} = \frac{P_{ac}}{E_{DC}} \tag{2.1}$$

Where P_{ac} is the active power exchanged between the VSC converter and the AC side. E_{DC} is the DC bus voltage and I_{DC} is the current provided by the converter.

2.4.2 Voltage source converter control

Once the converter model has been presented, in this section the control of the converter will be detailed. Next Figure 2.4 shows the control scheme for the converter.

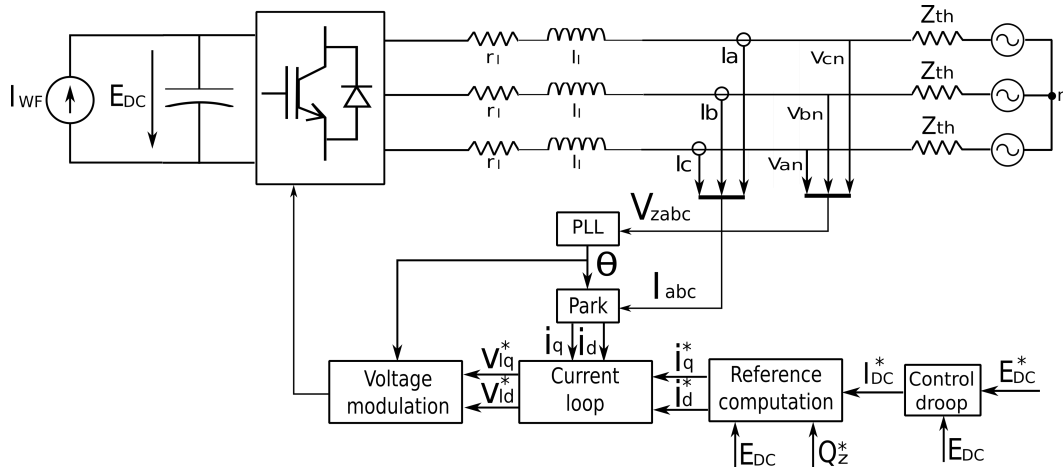


Figure 2.4: Voltage source converter control scheme

Note that the superscript $*$ indicates the set-point reference values. The currents and voltages involved in the control system are expressed in the synchronous reference frame $qd0$, through the Park transformation, which allows to convert the oscillating variables to constant quantities. Thus, the controller structure can be simplified as constant references must be tracked. A more detailed explanation of the Park transformation is explained in C.

The process starts with the reference voltage values of the DC bus and the reactive power flow. The first part, the Reference computation, compares the E_{DC}^* with the real value and, thanks to a proportional controller, the current reference for the AC grid is obtained. This current reference is the input of the next bloc, the current loop, in which a comparison and control of the desired current and the real one is done thanks to a PI controller. The output of the current loop is the necessary voltage reference that minimizes the error between the two above mentioned currents. It is worth to note that there are two loops, an inner loop that is the current loop and an outer loop that is the voltage loop. This will be worth for the control design, in Chapter 4.

The next step is doing the modulation, but as the model used is the averaged model, this step is skipped and the voltage references are directly applied by the voltage sources in the AC side.

Now, a more detailed explanation of each part of the system control is detailed below.

Droop control

As said in Chapter 1, for a multi-terminal system the type of controller used is typically a proportional controller, as the next expression denotes (2.2).

$$I_{DC}^* = K_{droop}(E_{DC} - E_{DC}^*) \quad (2.2)$$

As said before, the superscript $*$ indicates that the variable is a reference value. This expression (2.2) allows to obtain the reference current for the DC side of the converter (I_{DC}^*).

The technique shown in (2.2) is widely known as control droop. The implementation of the control droop is shown graphically in Figure 2.5.

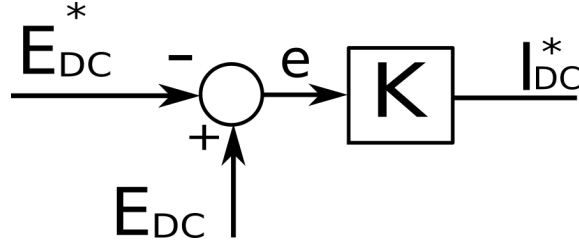


Figure 2.5: Droop control

Reference computation

The reference computation [3] allows to obtain the i_q^* and i_d^* current references from I_{DC}^* and Q^* . The main goal of the reference computation is to obtain i_q^* and i_d^* , which are the reference current values for the AC grid. To do so, since the model used is the averaged model, an active power balance between the AC and the DC side will allow to obtain i_q^* as expression (2.3) shows.

$$P_{dc} = E \cdot I_{DC}^* = P_{ac} = \frac{3}{2} v_{zq} \cdot i_q^* \quad (2.3)$$

Where V_z is the peak value for the AC grid which in this work is considered to be 320 kV. Regarding the reactive power, it is calculated using (C.5), that is, the equation for the reactive power when the Park transformation is applied as explained in C.

Once having seen the mathematical background, Figure 2.6 illustrates to implement it using a bloc scheme.

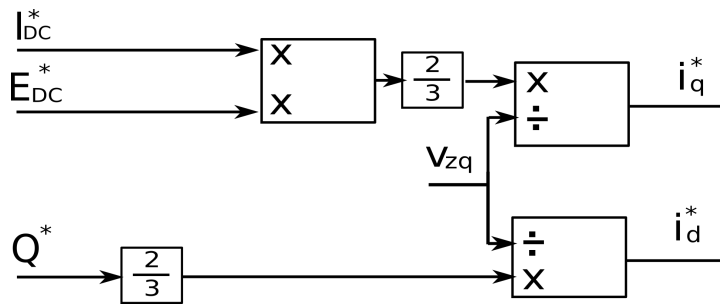


Figure 2.6: Reference computation

Current loop

The current loop design is based on the converter grid connection equations to the main AC grid [2]. Figure 2.7 shows the connection model describing the different system variables.

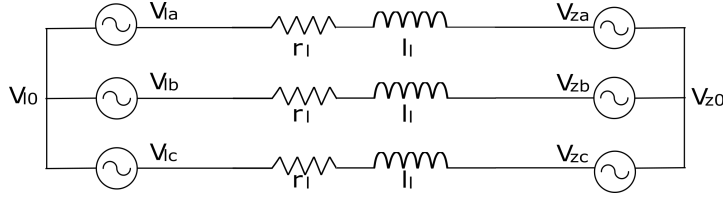


Figure 2.7: Connexion between the AC side of the converter and the AC grid

The subscript l refers to the variables of the converter side and the subscript z refers to grid variables. The electrical variables of the AC grid are represented by r_l and l_l . Then, the voltage equations are

$$\begin{bmatrix} v_{za} \\ v_{zb} \\ v_{zc} \end{bmatrix} - \begin{bmatrix} v_{la} \\ v_{lb} \\ v_{lc} \end{bmatrix} - (v_{0l} - v_{0z}) \begin{bmatrix} 1 \\ 1 \\ 1 \end{bmatrix} = \begin{bmatrix} r_l & 0 & 0 \\ 0 & r_l & 0 \\ 0 & 0 & r_l \end{bmatrix} \begin{bmatrix} i_a \\ i_b \\ i_c \end{bmatrix} + \begin{bmatrix} l_l & 0 & 0 \\ 0 & l_l & 0 \\ 0 & 0 & l_l \end{bmatrix} \frac{d}{dt} \begin{bmatrix} i_a \\ i_b \\ i_c \end{bmatrix} \quad (2.4)$$

As it is mentioned above, the current loop has the function to provide the voltage reference (v_{lq}^*) through two different PI controllers that are able to track the current references (i_{qd}^*) with the real current of the AC grid (i_{qd}).

By applying the Park transformation to equations (2.4), which illustrate the connexion between the AC side of the converter and the AC grid, the next system is obtained:

$$\begin{bmatrix} v_{zq} \\ 0 \end{bmatrix} - \begin{bmatrix} v_{lq} \\ v_{ld} \end{bmatrix} = \begin{bmatrix} r_l & l_l \omega_e \\ -l_l \omega_e & r_l \end{bmatrix} \begin{bmatrix} i_q \\ i_d \end{bmatrix} + \begin{bmatrix} l_l & 0 \\ 0 & l_l \end{bmatrix} \frac{d}{dt} \begin{bmatrix} i_q \\ i_d \end{bmatrix} \quad (2.5)$$

It is possible to assume $v_{zd} = 0$ V thanks to the PLL as it is described in the next section. From the equations, it can be seen that the q and d components of voltages and currents depend on each other so it seems to be impossible to control them separately. For that reason, the current controller could be designed using MIMO (Multiple Input Multiple Output) techniques. However, there is another possibility and that is the one used in this work. The technique consists in decoupling and independently controlling q and d components. Rewriting the system equations the next form is obtained:

$$\begin{bmatrix} v_{lq} \\ v_{ld} \end{bmatrix} = \begin{bmatrix} -\hat{v}_{lq} + v_{zq} - l_l \omega_e i_{ld} \\ -\hat{v}_{ld} - l_l \omega_e i_{lq} \end{bmatrix} \quad (2.6)$$

Where \hat{v}_{lq} and \hat{v}_{ld} are:

$$\begin{bmatrix} \hat{v}_{lq} \\ \hat{v}_{ld} \end{bmatrix} = \begin{bmatrix} r_l & 0 \\ 0 & r_l \end{bmatrix} \begin{bmatrix} i_q \\ i_d \end{bmatrix} + \begin{bmatrix} l_l & 0 \\ 0 & l_l \end{bmatrix} \frac{d}{dt} \begin{bmatrix} i_q \\ i_d \end{bmatrix} \quad (2.7)$$

Based on this decoupling the system can be seen as if it was compounded by two separated plants. Each plant is associated with a specific qd component and it is ideally independent

to the other plant. Transforming equations (2.5) into Laplace domain is possible to obtain the transfer function of each plant:

$$G_q(s) = \frac{i_q(s)}{\hat{v}_{lq}(s)} = \frac{1}{l_l s + r_l} \tag{2.8}$$

$$G_d(s) = \frac{i_d(s)}{\hat{v}_{ld}(s)} = \frac{1}{l_l s + r_l} \tag{2.9}$$

Figure 2.8 shows the control scheme for each current including the controllers $K_q(s)$ and $K_d(s)$. Notice that, as both plants are identical, both controllers will be equal.

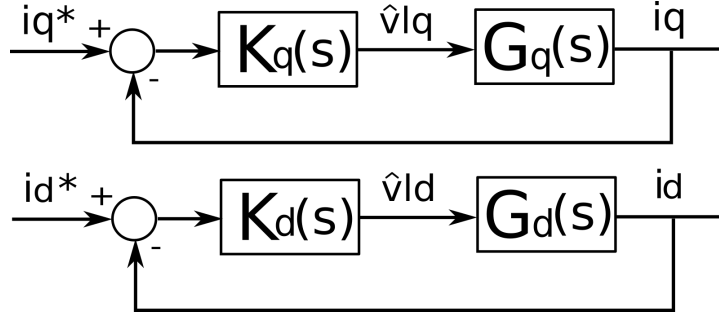


Figure 2.8: Current loop decoupled model

Taking this into account, the only thing that remains to be done is the controller design. Taking advantage that the mathematical expression of the plant is known, the design technique used is the Internal Model Control (IMC). The IMC allows to transform any dynamic system into a first order response using an integrator and the plant inverse. The next example will itemize this technique. Considering a generic feed-forward system formed by a plant $G(s)$ and a controller $K(s)$, the transfer function of the system is:

$$T = \frac{F(s)K(s)}{1 + G(s)K(s)} \tag{2.10}$$

Taking $K(s)$ as $\frac{\alpha}{s}G^{-1}(s)$ the transfer function takes the form:

$$T(s) = \frac{\frac{\alpha}{s}G^{-1}(s)G(s)}{1 + \frac{\alpha}{s}G^{-1}(s)G(s)} = \frac{\frac{\alpha}{s}}{1 + \frac{\alpha}{s}} = \frac{1}{\frac{s}{\alpha} + 1} = \frac{1}{\tau s + 1} \tag{2.11}$$

$$\frac{1}{\alpha} = \tau \tag{2.12}$$

A first order response is obtained and the time constant τ can be selected. In this case q plant (2.8) and d plant (2.9) are the same, so the controller will be the same as well:

$$G_q(s) = G_d(s) = \frac{\alpha}{s}G^{-1}(s) = \frac{l_l s + r_l}{s} = l_l \alpha + \frac{r_l \alpha}{s} \tag{2.13}$$

Note that the result is a proportional integral controller, where the constants are calculated as:

$$K_p = \frac{l_l}{\tau} \quad (2.14)$$

$$K_i = \frac{r_l}{\tau} \quad (2.15)$$

The implementation of these controllers in a decoupled design to compound the current loop is sketched in Figure 2.9.

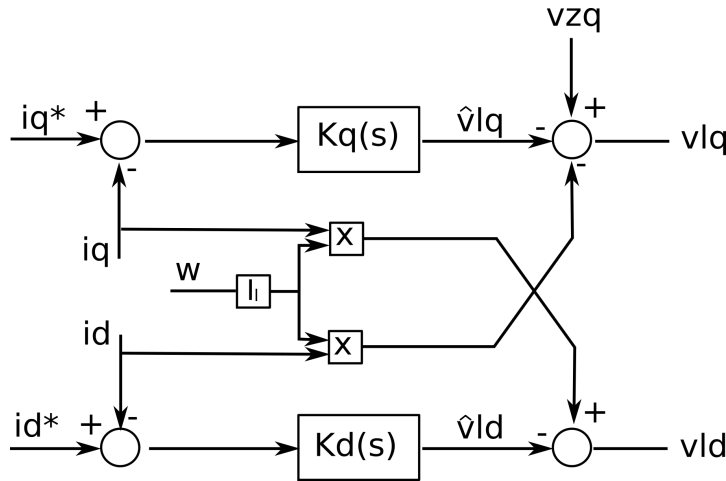


Figure 2.9: Current loop implementation

Phase locked loop

The phase locked loop, also known as PLL, has the function to determinate the angular velocity and the angle of the AC network. The general idea of the PLL [4] is illustrated in Figure 2.10.

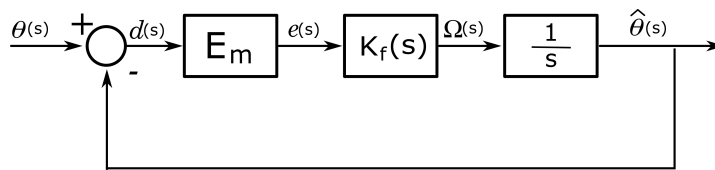


Figure 2.10: Phase locked loop general scheme

Where $\theta(s)$ is the real grid angle and $\hat{\theta}(s)$ is the angle tracked with the PLL. Thanks to $K_f(s)$, which is a proportional integral controller, the error will be zero. The mathematics behind this scheme will be detailed below. As it is explained in Annex C, the Park transformation (qd frame) is the Clark transformation ($\alpha\beta$ frame) plus a rotation, as next equation details:

$$\begin{bmatrix} v_q \\ v_d \end{bmatrix} = \begin{bmatrix} \cos \hat{\theta} & -\sin \hat{\theta} \\ \sin \hat{\theta} & \cos \hat{\theta} \end{bmatrix} \begin{bmatrix} v_\alpha \\ v_\beta \end{bmatrix} \quad (2.16)$$

Taking the v_d component the next expression is obtained:

$$v_d = v_\alpha \sin \hat{\theta} + v_\beta \cos \hat{\theta} = E_m \cos \theta \sin \hat{\theta} - E_m \sin \theta \cos \hat{\theta} \quad (2.17)$$

Where E_m is the peak voltage. By applying the sine subtract identity the above expression can be simplified:

$$v_d = E_m \sin \delta \quad (2.18)$$

$$\delta = \theta - \hat{\theta} \quad (2.19)$$

Assuming the difference between θ and $\hat{\theta}$ to be small, the above expression can be linearised:

$$v_d \approx E_m \delta = e \quad (2.20)$$

Taking into account the expression:

$$w = \frac{d\theta}{dt} = K_f \cdot e \quad (2.21)$$

Where K_f is the gain of the filter, all the variables in Figure 2.10 are explained. With all that, the transfer function of the system yields:

$$\frac{\hat{\theta}}{\theta} = \frac{E_m K_f(s)}{s + E_m K_f(s)} \quad (2.22)$$

For K_f , a generic form of a PI controller is taken:

$$K_f = K_p \left(\frac{1 + s\tau}{s\tau} \right) \quad (2.23)$$

Taking the generic form of a second order system and equalling term by term with the transfer function detailed above, it is possible to design the time response of the PLL as the next expressions denote.

$$\frac{\hat{\theta}}{\theta} = \frac{2\xi w_n s + w_n^2}{s^2 + 2\xi w_n s + w_n^2} \quad (2.24)$$

$$w_n = \sqrt{K_p E_m \tau} \quad (2.25)$$

$$\xi = \frac{K_p E_m}{2w_n} \quad (2.26)$$

Chapter 3

HVDC cable models

There exist a variety of models to represent the behaviour of a transition line. In this work the transitory state is simulated, therefore, the model has to take into account the capacitive and inductive characteristics of the line. Three models that comply this conditions are studied, these are the Pi model, the Pi coupled model and the Bergeron line model. In this section an explanation of each model is done.

3.1 Pi model

The Pi model [5] is sketched in Figure 3.1.

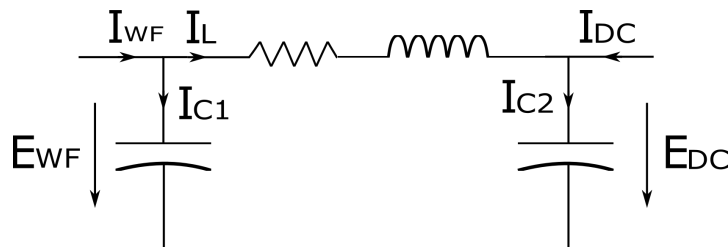


Figure 3.1: Pi model representation

It can be seen that the total inductance is gathered in one single element, the same occurs for the total resistance and the total capacitance, although the latter is distributed in two elements.

To study the Pi model it can be useful to see the cable as a MIMO system, where the two inputs are I_{WF} and I_{DC} , and the second one is a controlled input. The two outputs are the voltages at each end of the line and the purpose is to control the E_{DC} for a good performance of the converter. Seeing the line as a MIMO system allows to use the state-space representation, and that is useful to analyse the frequency response of the transitory state.

In a state-space representation of a system its equations are written in the form:

$$\dot{x} = Ax + Bu \quad (3.1)$$

$$y = Cx + Du \quad (3.2)$$

Where A,B,C and D are matrices, u and y are the respectively outputs and inputs vectors, and the x is a vector of the states of the system. Matlab Simulink allows to integrate this notation in a block in which the user has to introduce the matrices.

Before introducing the matrices the equations of the system are required. By applying the Kirchhoff's law in the mesh of Figure 3.1 the electric behaviour can be obtained.

$$I_{WF} = I_L + I_{C1} \quad (3.3)$$

$$I_{C2} = I_L + I_{DC} \quad (3.4)$$

$$\frac{dE_{WF}}{dt} = \frac{1}{C_1} \cdot (I_{WF} - I_L) \quad (3.5)$$

$$\frac{dE_{DC}}{dt} = \frac{1}{C_2} \cdot (I_{DC} + I_L) \quad (3.6)$$

$$\frac{dI_L}{dt} = \frac{E_{WF}}{L} - \frac{E_{DC}}{L} - R \cdot \frac{I_L}{dt} \quad (3.7)$$

Note that C_2 is C_1 plus the capacitance of the DC bus. By manipulating the expressions, the state-space notation is obtained.

$$\frac{d}{dt} \begin{bmatrix} I_L \\ E_{WF} \\ E_{DC} \end{bmatrix} = \begin{bmatrix} -\frac{R}{L} & \frac{1}{L} & -\frac{1}{L} \\ -\frac{1}{C_1} & 0 & 0 \\ \frac{1}{C_2} & 0 & 0 \end{bmatrix} \begin{bmatrix} I_L \\ E_{WF} \\ E_{DC} \end{bmatrix} + \begin{bmatrix} 0 & 0 \\ \frac{1}{C_1} & 0 \\ 0 & \frac{1}{C_2} \end{bmatrix} \begin{bmatrix} I_{WF} \\ I_{DC} \end{bmatrix} \quad (3.8)$$

$$\begin{bmatrix} E_{WF} \\ E_{DC} \end{bmatrix} = \begin{bmatrix} 0 & 1 & 0 \\ 0 & 0 & 1 \end{bmatrix} \begin{bmatrix} I_L \\ E_{WF} \\ E_{DC} \end{bmatrix} \quad (3.9)$$

Where in this case D is a zero matrix with suitable dimensions.

3.2 Pi model with multiple sections

It might be thought that a single Pi section is not a faithful representation of the reality because in the real line the electric properties are spread all along the cable. For more accuracy is possible to add Pi sections in series, but the more sections are added the higher is the number of variables. The electrical proprieties of the single original section are shared between the total number of components. A three section series is detailed below.

The equations of the system are:

$$I_{WF} = I_{L1} + I_{C1} \quad (3.10)$$

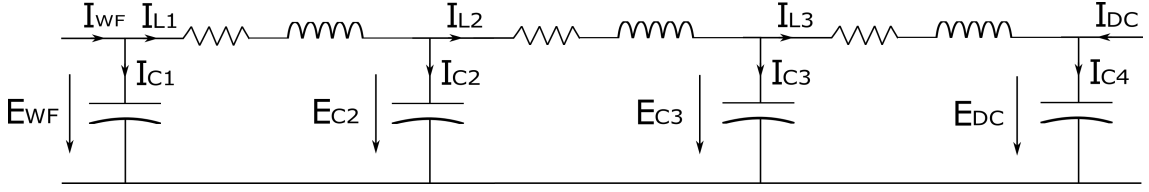


Figure 3.2: Three Pi model series representation

$$I_{L1} = I_{L2} + I_{C2} \quad (3.11)$$

$$I_{L2} = I_{L3} + I_{C3} \quad (3.12)$$

$$I_{C4} = I_{L3} + I_{DC} \quad (3.13)$$

$$\frac{dE_{WF}}{dt} = \frac{1}{C_1} \cdot (I_{WF} - I_{L1}) \quad (3.14)$$

$$\frac{dE_2}{dt} = \frac{1}{C_2} \cdot (I_{L1} - I_{L2}) \quad (3.15)$$

$$\frac{dE_3}{dt} = \frac{1}{C_3} \cdot (I_{L2} - I_{L3}) \quad (3.16)$$

$$\frac{dE_{DC}}{dt} = \frac{1}{C_4} \cdot (I_{DC} + I_{L3}) \quad (3.17)$$

$$\frac{dI_{L1}}{dt} = \frac{E_{WF}}{L} - \frac{E_2}{L} - R \cdot \frac{I_{L1}}{dt} \quad (3.18)$$

$$\frac{dI_{L2}}{dt} = \frac{E_2}{L} - \frac{E_3}{L} - R \cdot \frac{I_{L2}}{dt} \quad (3.19)$$

$$\frac{dI_{L3}}{dt} = \frac{E_3}{L} - \frac{E_{DC}}{L} - R \cdot \frac{I_{L3}}{dt} \quad (3.20)$$

Subsequently, the state-space notation is obtained. Note that for two consecutive sections its capacitors are added, so $C_2 = C_3 = 2 \cdot C_1$. It is recalled that C_4 is C_1 plus the DC bus capacitance.

$$\frac{d}{dt} \begin{bmatrix} I_{L1} \\ I_{L2} \\ I_{L3} \\ E_{WF} \\ E_2 \\ E_3 \\ E_{DC} \end{bmatrix} = \begin{bmatrix} -\frac{R}{L} & 0 & 0 & \frac{1}{L} & -\frac{1}{L} & 0 & 0 \\ 0 & -\frac{R}{L} & 0 & 0 & \frac{1}{L} & -\frac{1}{L} & 0 \\ 0 & 0 & -\frac{R}{L} & 0 & 0 & \frac{1}{L} & -\frac{1}{L} \\ -\frac{1}{C_1} & 0 & 0 & 0 & 0 & 0 & 0 \\ \frac{1}{C_2} & -\frac{1}{C_2} & 0 & 0 & 0 & 0 & 0 \\ 0 & \frac{1}{C_3} & -\frac{1}{C_3} & 0 & 0 & 0 & 0 \\ 0 & 0 & \frac{1}{C_4} & 0 & 0 & 0 & 0 \end{bmatrix} \begin{bmatrix} I_{L1} \\ I_{L2} \\ I_{L3} \\ E_{WF} \\ E_2 \\ E_3 \\ E_{DC} \end{bmatrix} + \begin{bmatrix} 0 & 0 \\ 0 & 0 \\ 0 & 0 \\ \frac{1}{C_1} & 0 \\ 0 & 0 \\ 0 & 0 \\ 0 & \frac{1}{C_4} \end{bmatrix} \begin{bmatrix} I_{WF} \\ I_{DC} \end{bmatrix} \quad (3.21)$$

$$\begin{bmatrix} E_{WF} \\ E_{DC} \end{bmatrix} = \begin{bmatrix} 0 & 0 & 0 & 1 & 0 & 0 & 0 \\ 0 & 0 & 0 & 0 & 0 & 0 & 1 \end{bmatrix} \begin{bmatrix} I_{L1} \\ I_{L2} \\ I_{L3} \\ E_{WF} \\ E_2 \\ E_3 \\ E_{DC} \end{bmatrix} \quad (3.22)$$

It can be seen that A matrix has a characteristic structure that can be extrapolated to a n Pi sections. This makes possible to program a script in Matlab with the generic form of the space-state matrices and allows the simulation of n Pi sections series with n as large as the computer calculation capacity allows.

3.3 Pi coupled model

In the previous sections, 3.2 and 3.1, the distributed nature of the cable parameters is taken into account, but there is still one important aspect missing, that is, the geometry of the cable itself [6]. As Figure 3.3 denotes, the internal structure of a HVDC cable is composed of different parts, and the main ones to consider are: the core, the first layer of insulator, and the screen.

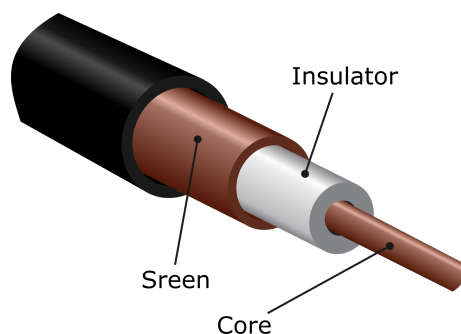


Figure 3.3: Scheme cable section

The core is the most internal part of the cable, and it is the medium in which the current travels through. It is usually made of copper although the material depends of the cable design. The electrical properties in the previous section are referred in this cable part. The first layer of insulator, as the name indicates, has the function to prevent the leakage of the current. Finally, the screen is a layer made of conductor material (normally made of copper, like the core) that is designed for insulating the electromagnetic field that generates the current when it travels through the core. These are the main parts that usually are present in every cable design. There exist other external layers, like for example, an extra layer of insulator thought to insulate the screen, an external layer made to strengthen the cable structure, or in the case a submarine cable (which is the case studied) there are layers made of waterproof materials in order to prevent the degradation due for example to the salinity levels of the water. Regarding to the electric behaviour of the cable, the effect of these last layers is minor compared to the effect of the core, but this assertion might not be true in the case of the screen layer. This is the goal of the coupled Pi model [7]; it takes into account the effect of the screen modelling it as an inductance coupled with the core inductance. The idea of this model is sketched in Figure 3.4

Once again, like in the Pi model the equations that describe the electric behaviour are deduced in order to obtain the space state representation.

$$\frac{du_{C1}}{dt} = \frac{1}{C}i_{C1} \quad (3.23)$$

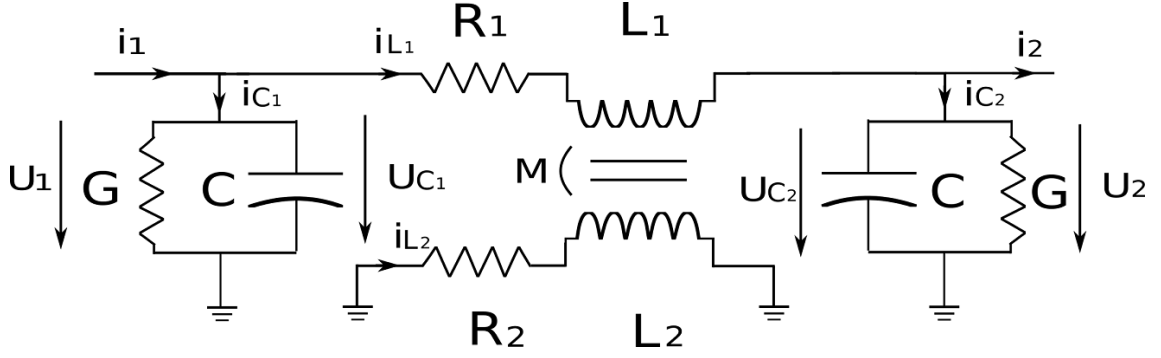


Figure 3.4: Coupled Pi model representation

$$\frac{du_{C2}}{dt} = \frac{1}{C}i_{C2} \quad (3.24)$$

$$\phi_1 = L_1i_{L1} + M_{12}i_{L2} \quad (3.25)$$

$$\phi_2 = L_2i_{L2} + M_{21}i_{L1} \quad (3.26)$$

$$u_{L1} = \frac{d\phi_1}{dt} = L_1 \frac{di_{L1}}{dt} + M_{12} \frac{di_{L2}}{dt} \quad (3.27)$$

$$u_{L2} = \frac{d\phi_2}{dt} = L_2 \frac{di_{L2}}{dt} + M_{21} \frac{di_{L1}}{dt} \quad (3.28)$$

Combining (3.27) and (3.28) and taking into account that $M_{12} = M_{21}$:

$$\frac{di_{L1}}{dt} = \frac{u_{L1}L_2}{L_1L_2 - M_{12}^2} - \frac{u_{L2}M_{12}}{L_1L_2 - M_{12}^2} \quad (3.29)$$

$$\frac{di_{L2}}{dt} = \frac{u_{L2}L_1}{L_1L_2 - M_{12}^2} - \frac{u_{L1}M_{12}}{L_1L_2 - M_{12}^2} \quad (3.30)$$

Taking into account that:

$$i_{C1} = -i_1 - i_{L1} - Gu_{C1} \quad (3.31)$$

$$i_{C2} = -i_2 - i_{L2} - Gu_{C2} \quad (3.32)$$

$$U_{L1} = -R_1i_{L1} - u_{C2} + u_{C1} \quad (3.33)$$

$$u_{L2} = -R_2i_{L2} \quad (3.34)$$

Rearranging the above expressions the space state of the model can be obtained and it has the form:

$$\frac{d}{dt} \begin{bmatrix} u_{C1} \\ u_{C2} \\ i_{L1} \\ i_{L2} \end{bmatrix} = \begin{bmatrix} -\frac{G}{C} & 0 & -\frac{1}{C} & 0 \\ 0 & -\frac{G}{C} & -\frac{1}{C} & 0 \\ \frac{L_2}{L_1L_2 - M_{12}^2} & -\frac{L_2}{L_1L_2 - M_{12}^2} & -\frac{R_1L_2}{L_1L_2 - M_{12}^2} & \frac{R_2M_{12}}{L_1L_2 - M_{12}^2} \\ -\frac{M_{12}}{L_1L_2 - M_{12}^2} & \frac{M_{12}}{L_1L_2 - M_{12}^2} & \frac{R_1M_{12}}{L_1L_2 - M_{12}^2} & -\frac{R_2L_1}{L_1L_2 - M_{12}^2} \end{bmatrix} \begin{bmatrix} u_{C1} \\ u_{C2} \\ i_{L1} \\ i_{L2} \end{bmatrix} + \begin{bmatrix} -\frac{1}{C} & 0 \\ 0 & -\frac{1}{C} \\ 0 & 0 \\ 0 & 0 \end{bmatrix} \begin{bmatrix} I_1 \\ I_2 \end{bmatrix} \quad (3.35)$$

$$\begin{bmatrix} u_1 \\ u_2 \end{bmatrix} = \begin{bmatrix} 1 & 0 & 0 & 0 \\ 0 & 1 & 0 & 0 \end{bmatrix} \begin{bmatrix} u_{C1} \\ u_{C2} \\ i_{L1} \\ i_{L2} \end{bmatrix} \quad (3.36)$$

3.4 Bergeron line model

In the previous section 3.2 it can be seen that the Pi model can be more accurate if multiple Pi sections are added. However, the Bergeron line model takes into account the distributed nature of the electrical properties of the line starting from a different point of view [8], [9].

Instead of adding multiple sections, the Bergeron model consists in taking a differential line section and obtaining its differential equations. By solving the equations system a general equation for the Voltage and the Current can be obtained. That makes possible to implement the equations in Matlab and doing simulations in aim to study the transient state. Matlab Simulink incorporates a bloc called *Distributed parameter line* in where the Bergeron model is implemented and it is used along this work in various simulations.

However, in this Matlab bloc there is a particular way in where the Bergeron equations are implemented. Instead of considering the resistance from the beginning, Matlab considers the Bergeron equations with no resistive components. This simplification makes the implementation of the Bergeron equations much more easier, but not realistic. For that reason, to take into account the resistance Matlab simulates its value in a similar way to the Pi model, that is, gathering the total resistance in one element (it is really gathered in three elements, but this will be explained later).

Once having seen all these points, an explanation of the origin of the Bergeron equation and its implementation in Matlab is done. As mentioned above, the derivation starts taking a differential of lossless line cable and obtaining the differential equations as Figure 3.5 shows.

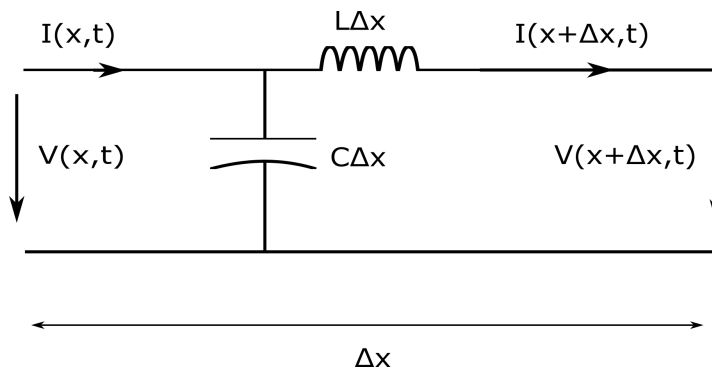


Figure 3.5: Differential of cable

$$V(x + \Delta x, t) = V(x, t) - L \Delta x \frac{\partial I(x + \Delta x, t)}{\partial t} \quad (3.37)$$

$$I(x, t) = I(x + \Delta x, t) + C \Delta x \frac{\partial V(x, t)}{\partial t} \quad (3.38)$$

Rearranging the above expressions:

$$\frac{V(x + \Delta x, t) - V(x, t)}{\Delta x} = -L \frac{\partial I(x + \Delta x, t)}{\partial t} \quad (3.39)$$

$$\frac{I(x + \Delta x, t) - I(x, t)}{\Delta x} = -C \frac{\partial V(x, t)}{\partial t} \quad (3.40)$$

Note that in both left side of the above expressions, taking $\Delta x \rightarrow 0$ it corresponds to the definition of derivation, so the equations can be rewritten.

$$\frac{\partial V(x, t)}{\partial x} = -L \frac{\partial I(x, t)}{\partial t} \quad (3.41)$$

$$\frac{\partial I(x, t)}{\partial x} = -C \frac{\partial V(x, t)}{\partial t} \quad (3.42)$$

These equations are known as telegraph equations. Differentiating (3.41) respect to x and (3.42) respect to t the above equations take the form:

$$\frac{\partial^2 V(x, t)}{\partial x^2} = -L \frac{\partial^2 I(x, t)}{\partial x \partial t} \quad (3.43)$$

$$\frac{\partial^2 I(x, t)}{\partial x \partial t} = -C \frac{\partial^2 V(x, t)}{\partial t^2} \quad (3.44)$$

By substituting (3.44) into (3.43) the next equality is obtained:

$$\frac{\partial^2 V(x, t)}{\partial x^2} = LC \frac{\partial^2 V(x, t)}{\partial t^2} \quad (3.45)$$

Similarly, differentiating (3.41) respect to t and (3.42) respect to x , and like illustrated above, substituting the two obtained expressions, the next current relation is obtained:

$$\frac{\partial^2 I(x, t)}{\partial x^2} = LC \frac{\partial^2 I(x, t)}{\partial t^2} \quad (3.46)$$

Note that (3.45) and (3.46) have the form $u_{tt} - c^2 u_{xx} = 0$ that corresponds to the one-dimensional wave equation. The solution of this equation is obtained with Alembert formula, and applying it in the above expressions the general solution is obtained.

$$I(x, t) = i^+(x - vt) + i^-(x + vt) \quad (3.47)$$

$$V(x, t) = v^+(x - vt) + v^-(x + vt) \quad (3.48)$$

Where v is the velocity propagation in [m/s], which corresponds to $v = \frac{1}{\sqrt{LC}}$

The functions i^+, i^-, v^+ and v^- are arbitrary current/voltage time dependent functions. The superscript $+$ indicates that the wave travels in the positive sense of the x axis, and $-$ indicates the negative sense. The point of these functions is that they represent waves that move forward or backward at speed v and maintain their shape during the travel. The waveform is also defined by the above mentioned functions. Note that these model consist in a superposition of forward and backward waves, for that reason the Bergeron model is also known as Bergeron travelling wave model.

Continuing with the explanation of the Bergeron model, once the general solution is obtained, the voltage equation (3.48) can be rewritten in terms of i^+ and i^- :

$$V(x, t) = Z_c[i^+(x - vt) - i^-(x + vt)] \tag{3.49}$$

Where $Z_c = \sqrt{\frac{L}{C}}$ is the characteristic impedance of the line. By adding $Z_c I(x, t)$ at both sides of the voltage equation the expression obtained is:

$$V(x, t) + Z_c I(x, t) = 2Z_c i^+(x - vt) \tag{3.50}$$

The key point in the Bergeron model is that looking in the right side of (3.50), the term $(x - vt)$ remains constant to a reference travelling at the same speed v of the wave. Taking that into account, the next relationship can be obtained:

$$V_k(t - \tau) + Z_c I_{k,m}(t - \tau) = V_m(t) - Z_c I_{m,k}(t) \tag{3.51}$$

Where τ is the time that takes for the wave to go from the beginning to the end of the line. This time can be calculated if the length line and the travelling speed are known. Recalling from (3.4), and given a length l , the travelling time is:

$$\tau = \frac{l}{v} = \frac{l}{\sqrt{LC}} \tag{3.52}$$

Once having seen τ , the next Figure 3.6 will help to understand the reasoning applied for obtaining the above expression (3.51).

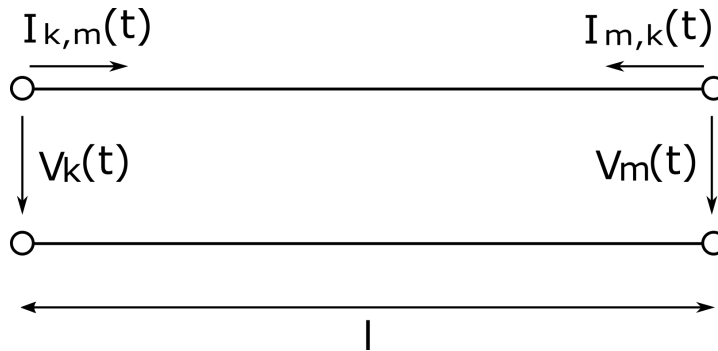


Figure 3.6: k,m notation

Considering a wave that leaves the node k at time $(t - \tau)$, as explained above, if a reference that travels next to the wave at speed v is considered, the wave will be seen as constant during all the travelling process. This allows to affirm that the wave that leaves the node k at time $(t - \tau)$ is the same wave that reaches the node m at time t . This makes possible to obtain a mathematical relation between the nodes k and m in terms that are calculated in different time points, like the above expression denotes (3.51). By applying the same procedure in the reverse path, that is, the travel from m to k a similar expression is obtained (3.53).

$$V_m(t - \tau) + Z_c I_{m,k}(t - \tau) = V_k(t) - Z_c I_{k,m}(t) \quad (3.53)$$

Rearranging the equations (3.51) and (3.53), the next current expressions can be obtained.

$$I_{k,m}(t) = \frac{V_k(t)}{Z_c} - \frac{V_m(t - \tau)}{Z_c} - I_{k,m}(t - \tau) \quad (3.54)$$

$$I_{m,k}(t) = \frac{V_m(t)}{Z_c} - \frac{V_k(t - \tau)}{Z_c} - I_{m,k}(t - \tau) \quad (3.55)$$

The above expressions can be simplified using the notation:

$$I_k(t - \tau) = -\frac{V_m(t - \tau)}{Z_c} - I_{k,m}(t - \tau) \quad (3.56)$$

$$I_m(t - \tau) = -\frac{V_k(t - \tau)}{Z_c} - I_{m,k}(t - \tau) \quad (3.57)$$

This notation allows to view the model as a Norton equivalent as Figure 3.7 shows, and that facilitates the PC implementation.

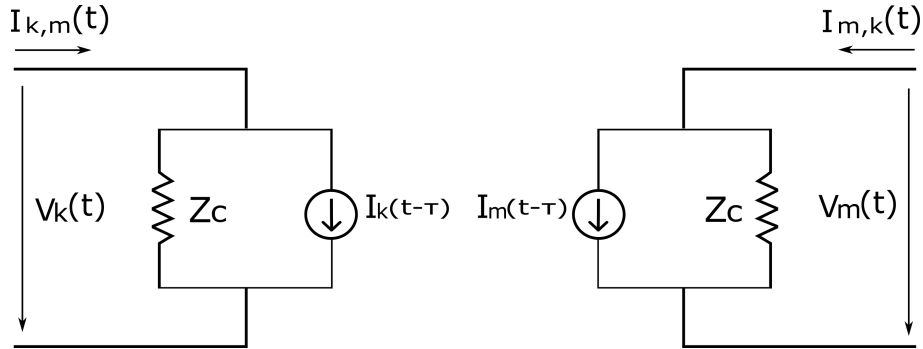


Figure 3.7: Norton equivalent for the Bergeron model implementation

Note that the current source involves past values that are used to calculate the actual values. Moreover, this actual values will be stored to calculate future values. It can be seen that this is an iterative process that a computer can do starting from an initial state that can be introduced at the beginning of the calculation. This is how the Matlab bloc *Distributed parameter line* works. However, the resistance is still missing. When a

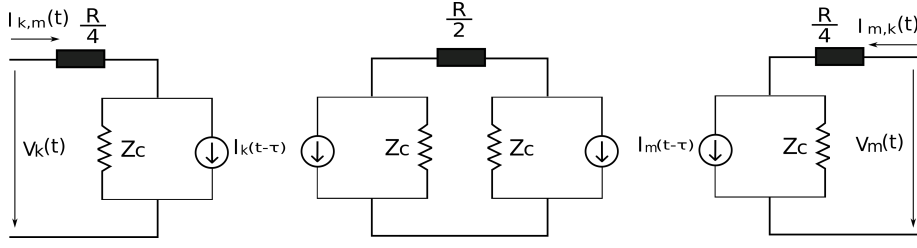


Figure 3.8: Norton equivalent when a lossy line is considered

lossy line is considered (which is almost always the case) Matlab combines two Norton equivalents and three blocs that represent the total resistance as Figure 3.8 denotes.

This, as said above, allows to consider the resistance in a similar way that the Pi model does. The derivation of the equations of Figure 3.8 extend to much for the main aim of this work, for this reason the derivation and its equations are not explained. Furthermore, Matlab does not even work directly with the structure showed in Figure 3.8, it rearranges the equations from Figure 3.8 in order to make them compatible with the structure showed in Figure 3.7, that is, a single Norton equivalent but with different equations for Z_c and the current sources. In other words, the mathematical background is the one behind the model in Figure 3.8 but with a rearrangement that makes it compatible with the structure in Figure 3.7.

Calling R the total resistance of the cable, the final equations in which Matlab actually works result:

$$I_k(t-\tau) = \left(\frac{1+h}{2}\right) \left(\frac{1+h}{Z_c} V_m(t-2\tau) - h I_{m,k}(t-2\tau)\right) + \left(\frac{1-h}{2}\right) \left(\frac{1+h}{Z_c} V_k(t-2\tau) - h I_{k,m}(t-2\tau)\right) \quad (3.58)$$

$$I_m(t-\tau) = \left(\frac{1+h}{2}\right) \left(\frac{1+h}{Z_c} V_k(t-2\tau) - h I_{k,m}(t-2\tau)\right) + \left(\frac{1-h}{2}\right) \left(\frac{1+h}{Z_c} V_m(t-2\tau) - h I_{m,k}(t-2\tau)\right) \quad (3.59)$$

$$Z_c = Z_c + \frac{R}{4} \quad (3.60)$$

$$h = \frac{Z_c - \frac{R}{4}}{Z_c + \frac{R}{4}} \quad (3.61)$$

Here the explanation of the Bergeron model concludes. It should be noted that during the study of this model it was found that there was another model called *Distributed parameter model* that has many similarities with the Bergeron model. Both of them start with the same idea of analysing a differential of cable in order to take into account its distributed nature. The difference, however, is that in some point the treatment of the differentials equations is not the same and also differs the setting of its initial conditions. That makes that the final result is apparently different from the Bergeron model. A more detailed approach is explained in D in which is shown that the two models are the same. It was deemed appropriate to clarify this to not create confusion.

Chapter 4

Control design

4.1 Justification of the type of controller used

The variable to be controlled is the DC grid voltage. The type of controller used to achieve this purpose is the droop control, described in Chapter 1.

As explained before in Chapter 1 and in Chapter 2, droop control is widely accepted for the DC voltage control of multi-terminal grid. However, as this work is focused on the impact of the cable model into the design of the droop control, the selected case study is a two-terminal grid, to simplify the analysis. However, the conclusions extracted from the two-terminal analysis can be extrapolated to a multi-terminal case.

Wind Farm

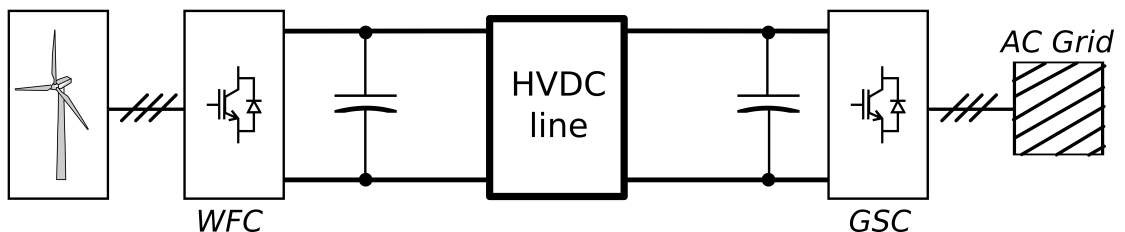


Figure 4.1: General scheme for the two terminals case

4.2 Control design assumptions

First, it must be mentioned that the DC grid voltage control is performed by the AC grid side converter, whereas the wind farm converter is considered to be injecting the generated power from the wind farm.

Before determining the appropriate value of the proportional constant of the controller (K_{droop}), some assumptions in the system will be made to facilitate the control design [10]. Figure 2.4 explains the two different control loops present in the converter, the inner current loop and the outer voltage droop control loop. The dynamics of the current loop

are considered to be much faster than the voltage loop ones. For that reason, for the corresponding study the current loop response is considered instantaneous, which means that the corresponding outer loop will be designed without considering the dynamics of current loop, as is sketched in Figure 4.2.

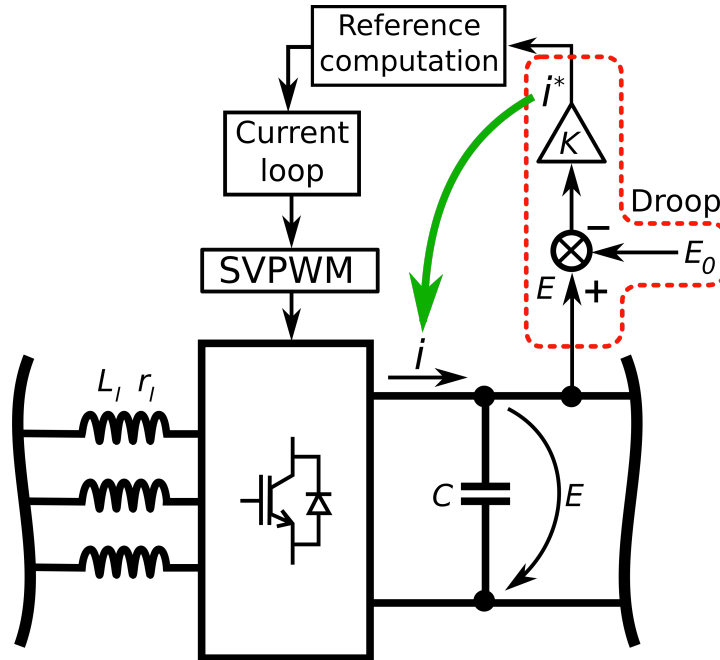


Figure 4.2: Simplification of the current loop at the AC grid side converter

Considering that, and since the model used to study the converter is the averaged model in where the switchings are neglected, the system in which the control design will be studied is sketched in Figure 4.3.

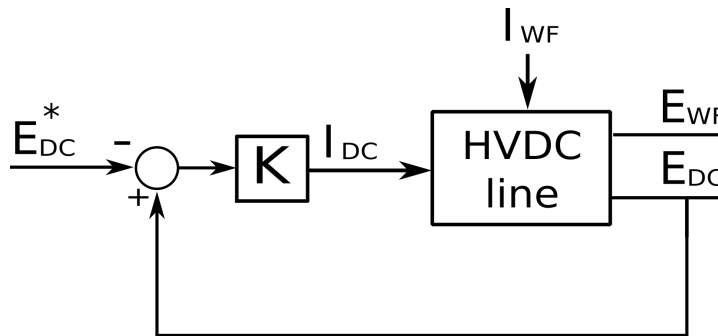


Figure 4.3: Simplified model

It can be seen that the output of the controller, as said before, is directly the current applied by the converter. The plant is the model used to simulate the HVDC line, in which the inputs are the current provided by the converter and the current of the wind farm that plays the role of disturbance due to its variable nature. As outputs, there are the voltage in the wind farm side, and the voltage in the converter side which is the controlled

output. Note that the bus capacitances of each side of the line are taken into account inside the line model.

4.3 Control problem definition

In previous chapters, the cable modelling has been oriented to obtain an state space model. Next, this model will be employed to obtain the transfer functions of the system which will be useful to design the droop voltage controller. The Figure 4.4 will help to understand the notation used.

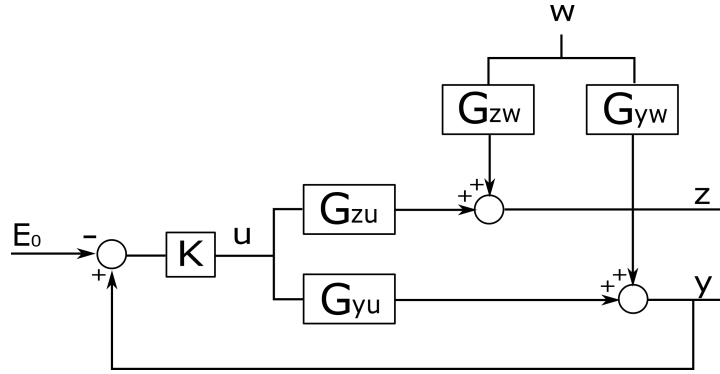


Figure 4.4: Notation of simplified model

Where $w(s)$ is the wind farm current I_{WF} that acts as disturbance, $u(s)$ is the current injected by the converter I_{DC} , $z(s)$ is the wind farm voltage E_{WF} , and $y(s)$ is the voltage of the DC bus E_{DC}

$G_{zw}(s)$ is the transfer function that relates the input w to the output z

$G_{yw}(s)$ is the transfer function that relates the input w to the controlled output y

$G_{zu}(s)$ is the transfer function that relates the input u to the output z

$G_{yu}(s)$ is the transfer function that relates the input u to the controlled output y

This set of transfer functions form the MIMO system for the cable model. Note that, this notation is also valid for an n terminal system [10], in which case, the above mentioned transfer functions would be matrices of transfer functions, and the inputs and outputs would be vectors. Due to the space state representation of the cable model is known, the above mentioned transfer functions can be found using [11], [12]:

$$G_{zw}(s) = C_z(sI - A)^{-1}B_w \quad (4.1)$$

$$G_{yw}(s) = C_y(sI - A)^{-1}B_w \quad (4.2)$$

$$G_{zu}(s) = C_z(sI - A)^{-1}B_u \quad (4.3)$$

$$G_{yu}(s) = C_y(sI - A)^{-1}B_u \quad (4.4)$$

In the state-space notation, A is the state matrix, B is a matrix that relates the inputs with the states, and C is a matrix that relates the states with the outputs. In the above expressions the sub-index in the C and B matrices indicates the input or output in which the matrix is referred to. For example, recalling the expression of the outputs of one single Pi section showed above (3.9), the expression was:

$$y = \begin{bmatrix} E_{WF} \\ E_{DC} \end{bmatrix} = \begin{bmatrix} 0 & 1 & 0 \\ 0 & 0 & 1 \end{bmatrix} \begin{bmatrix} I_L \\ E_{WF} \\ E_{DC} \end{bmatrix} \quad (4.5)$$

In this case, the C_w matrix refers to the part of matrix C that contributes to the output $w(s)$ (that is, the wind farm current), and its expression would be:

$$C_w = [0 \quad 1 \quad 0] \quad (4.6)$$

Note that no matters how complex the two-terminal line model is provided that it has the two right inputs and the two right outputs, in other words, the above expressions have the same form for the Pi sections model with 10 sections than for n sections. Furthermore, these expressions are also valid for any other model provided that it is expressed in space state notation, such for example the Pi coupled model studied in this work.

Once the system to be controlled has been presented, the droop voltage control gain must be selected. As said before, in a proportional control the existence of error is inevitable, but this error could be limited to a certain value. This limitation on the error value will help to determine the K_{droop} . First of all, it is necessary to obtain the error expression, recalling from Figure 4.4 the expression results:

$$e(s) = y(s) - E_0(s) \quad (4.7)$$

To obtain the function $y(s)$ it is necessary to find first the effect that $E_0(s)$ has on $y(s)$ and the effect of $w(s)$ in $y(s)$ and apply the superposition principle.

$$y(s) = -G_{yu}(s)K(I - G_{yu}(s)K)^{-1}E_0(s) + G_{yw}(s)(I - G_{yu}(s)K)^{-1}w(s) \quad (4.8)$$

Defining $S(s) = (I - G_{yu}(s)K)^{-1}$ as the sensitivity function, the resulting expression is:

$$y(s) = -G_{yu}(s)KS(s)E_0(s) + G_{yw}(s)S(s)w(s) \quad (4.9)$$

By substituting (4.9) into (4.7) and rearranging the expression the result is:

$$e(s) = G_{yw}(s)S(s)w(s) - S(s)E_0(s) \quad (4.10)$$

The term $S(s)E_0(s)$, although it appears in (4.10) it actually does not have any effect on the error value [10]. $E_0(s)$ is a constant reference so it only affects the error when $s = 0$, and for any other value of $s \neq 0$ the value of the reference is zero. Furthermore, the

sensitivity function $S(s)$ is zero when $s = 0$. This implies that when $E_0(0) \neq 0 \rightarrow S(0) = 0$ and vice versa, thereby, the term $S(s)E_0(s)$ is always zero. Taking that into account, is possible to write:

$$e(s) = G_{yw}(s)S(s)w(s) \quad (4.11)$$

First, an analysis of the steady state is carried out. It implies that $s \rightarrow 0$ as it corresponds to $t \rightarrow \infty$ in time domain. The above expression considered in the steady state case is:

$$\frac{e(0)}{w(0)} = G_{yw}(0)S(0) = \frac{1}{K_{droop}} \quad (4.12)$$

Note that, this can be very useful in order to design the controller, without considering the system dynamics. By accepting a fixed maximum value of error (maximum voltage error) and considering an maximum value disturbance (maximum current coming from the wind farm), a valid value for the K_{droop} in steady state that maintains the voltage below the defined limit can be found. This would be studied and discussed in the next chapter, in where a frequency analysis will be done, and a stability study will be detailed.

Chapter 5

Controller frequency analysis

In this section a frequency analysis is done for each model, except for the Bergeron one that is used as reference in order to validate the other models. This comparison is described in Chapter 6. The models analysed in this section are: the Pi model, the Pi model with multiple sections and the coupled Pi model.

First, the systems parameters of the system under analysis are detailed and a first approach for the droop calculation is done using the steady state considerations. Before explaining the frequency analysis, a brief explanation of the methodology used is included.

5.1 System parameters and droop calculation for steady state case

Before designing the droop control it is necessary to numerically define the parameters involved in the system studied. The electrical parameters considered for the HVDC grid are described in [7]. For the AC grid parameters the values used are the ones from the CIGRÉ model [1]. Regarding the converter characteristics, it is used [5] as example. All the mentioned parameters are gathered in Table 5.1.

Taking into account all the system parameters, it is possible to calculate the droop value using the steady state approach made in Chapter 4. Recalling from (4.12), at steady state, the relation between the voltage error in front the current provided by the converter is:

$$\frac{e(0)}{w(0)} = \frac{1}{K_{droop}} \quad (5.1)$$

Considering an error of 10% the nominal bus voltage, that is 40 kV, and a perturbation as the nominal current of the converter, which is 875 A, the K_{droop} value that satisfies the error conditions at steady state is $K_{droop} = \frac{1}{45}$.

Parameter	Value	Units
S_{base} for the AC grid	526	MVA
V_{base} for the AC grid	320	kV
R_{pu} for the AC grid	0,01	pu
L_{pu} for the AC grid	0,15	pu
R for the HVDC grid	5,3	$\frac{m\Omega}{km}$
L for the HVDC grid	3,6	$\frac{mH}{km}$
C for the HVDC grid	0,24	$\frac{\mu F}{km}$
R_{screen} for the HVDC grid in Pi coupled model	60,2	$\frac{m\Omega}{km}$
L_{screen} for the HVDC grid in Pi coupled model	3,5	$\frac{mH}{km}$
M for the HVDC grid in Pi coupled model	3,5	$\frac{mH}{km}$
C_{BUS}	150	μF
HVDC line distance	200	km
Time constant for the current loop	10	ms
Reference value for the DC bus	400	kV
Reference value for the reactive power	0	W
VSC converter power	350	MW
Nominal value for the current converter	875	A

Table 5.1: System parameters

5.2 Methodology description

Recalling the notation used and explained in section 4.3, the frequency analysis will be focused in studying the transfer function relating the current input from the wind farm and the error voltage $S(s)G_{yw}(s)$, besides the transfer function relating again the current from the wind farm and the current of the grid side converter $KS(s)G_{yw}(s)$. This frequency analysis will consist in a Bode representation of this so-mentioned functions for all the frequency range, focusing on the gain plot. The reason to study specifically $S(s)G_{yw}(s)$ and $KS(s)G_{yw}(s)$ is detailed below.

In the case of $S(s)G_{yw}(s)$, recalling from (4.11) its transfer function is detailed below.

$$\frac{e(s)}{w(s)} = G_{yw}(s)S(s) \quad (5.2)$$

Where S is the sensitivity function defined in (4.3). The reason to study $S(s)G_{yw}(s)$ is the same as the approach made in Chapter 4, but instead of using (5.1) to set the error limit a Bode diagram will be used in where this limitation will be specified graphically.

This Bode representation will be done with different values of K_{droop} , using the value found considering the steady state as order of magnitude. The point is to find out if there is some frequency in which the system has a gain that exceeds the error specifications. As will be seen later, the study of this function will be useful in order to find an lower limit value for the K_{droop} .

Regarding the interest in the analysis of $KS(s)G_{yw}(s)$, the transfer function can be seen below (5.3).

$$\frac{u(s)}{w(s)} = KG_{yw}(s)S(s) \quad (5.3)$$

The idea of studying this transfer function is similar to the one before. Observing its behaviour at high frequencies will allow to find if there exists some frequency value that produces an excessive gain that exceeds the current rating of the converter. Advancing results, it will be seen that this analysis will allow to find an upper limit for the K_{droop} value, and with that, a range of valid values for the K_{droop} can be found.

Here, the criteria to decide if a certain gain is excessive will be the physical maximum current characteristics of the converter, namely the nominal current value. This criterion translated into mathematical language is that $KS(s)G_{yw}(s)$ has not a gain bigger than one (or 0 dB) in all its frequencies [10]. This limitation will be seen graphically in the Bode diagrams done for $KG_{yw}(s)S(s)$. Of course, analogously to the study of $G_{yw}(s)S(s)$, different values for the K_{droop} are plotted to deduce which are the most suitable constants for the system.

However, all these criteria will be useless if the system is unstable. For that reason first of all, before doing the frequency analysis, a stability study is carried out for the different values of K_{droop} . As said before, first of all an stability analysis is done. The condition that a system has to accomplish to be stable is that all the real parts of the system poles have to be negative [11]. In a space state notation it is known that the eigenvalues of the A matrix are the same as the system poles [12]. However, as the analysis is focused in the closed loop system employing droop control, the eigenvalues of the closed loop matrix must be obtained [10], as:

$$A_{cl} = A + K_{droop}B_uC_y \quad (5.4)$$

This process is done in all the stability analysis presented along this work, so this explanation will not be repeated again.

Next, the analysis of the previous mentioned cable models is detailed below.

5.3 Pi model analysis

5.3.1 Stability analysis

It is clear that A_{cl} depends on the K_{droop} value, for that reason, this stability analysis is done for different values as Figure 5.1 illustrates.

It can be seen that there are not positive eigenvalues for the closed loop A matrix, so the system is stable as expected.

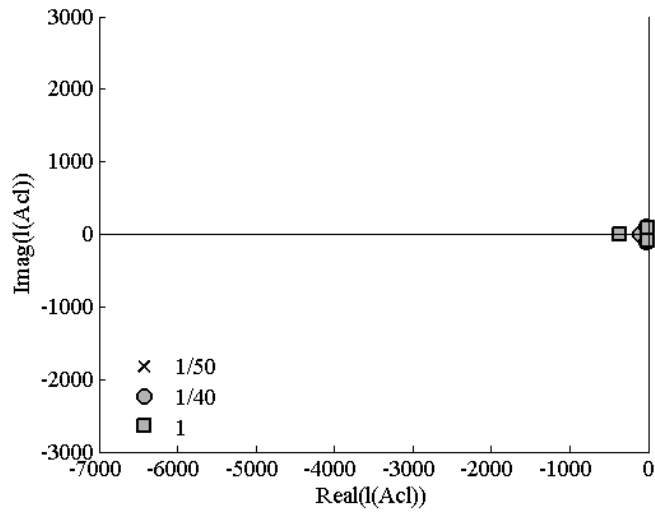


Figure 5.1: Stability analysis for 1 Pi section

5.3.2 Frequency analysis

Once having seen that the system is stable, Figure 5.2 shows the Bode diagram for $S(s)G_{yw}(s)$.

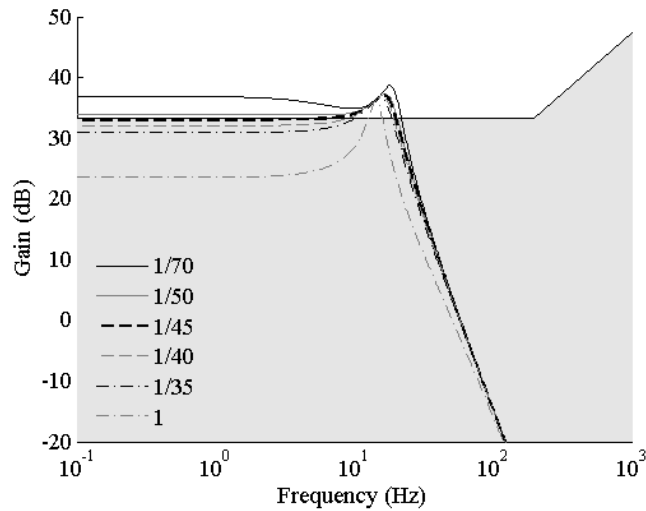


Figure 5.2: Bode diagram for $S(s)G_{yw}(s)$

And the next Figure 5.3 the Bode diagram for $KS(s)G_{yw}(s)$.

The shadowed area is the region where the conditions of maximum error and current are accomplished. In the case of 5.2, the limitation is imposed by the maximum error specification, and for Figure 5.3, the limitation is imposed by the maximum allowed current. Both limitations are calculated assuming a nominal current input coming from the wind farm. The study is done for higher and lower values than $\frac{1}{45}$.

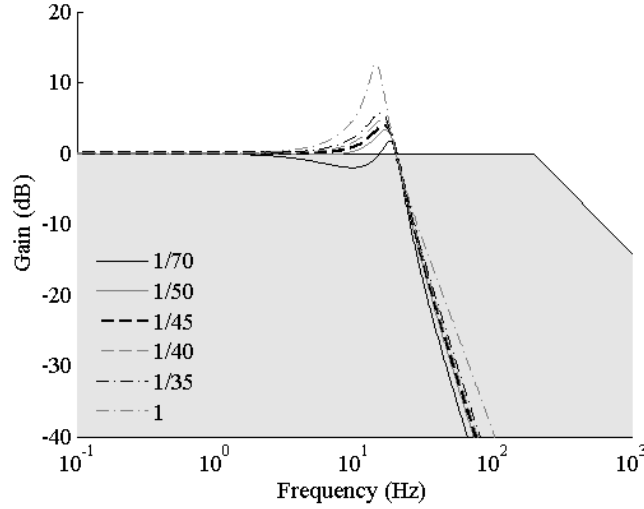


Figure 5.3: Bode diagram for $KS(s)G_{yw}(s)$

The first thing to denote is that for frequencies near to 10 Hz the above specified conditions are not fulfilled. By observing the two graphics, it can be seen that they represent two conflicting objectives. Starting for example for Figure 5.2 it can be seen that the higher the K_{droop} is, the better the conditions are satisfied. Taking $K_{droop} = 1$ for example, the error limitation is still exceeded, but there is an improvement because the gain is lower. Assuming higher values of K_{droop} will contribute to minimize the error. This can be seen in the previous section where a study is done for the steady state case. It can be seen that the K_{droop} is inversely proportional to the gain of $S(s)G_{yw}(s)$.

$$\frac{e(0)}{w(0)} = G_{yw}(0)S(0) = \frac{1}{K_{droop}} \quad (5.5)$$

However, by observing the second Figure 5.3 it can be seen that the higher is the K_{droop} , the worse is the fulfilment of the second condition. Higher values of K_{droop} cause higher gains for $KS(s)G_{yw}(s)$. This is the reason that the study of $S(s)G_{yw}(s)$ and $KS(s)G_{yw}(s)$ show conflicting objectives. However, it is possible to take advantage of this in order to specify a range of valid values for the K_{droop} , and as it is mentioned before, the study of the above mentioned transfer functions will be useful in order to set an lower and an upper limit for the aforementioned range.

According to this model, it does not seem possible to find an appropriate value of K_{droop} , because all the values represented in Figure 5.2 and Figure 5.3 exceed the imposed limit conditions in each graphic. The point here is to determine the significance that have the gains that appear at about 10 Hz frequency. To judge that, some considerations have to be done.

First of all, in the wind farm side there is another converter with similar characteristics as the AC grid side converter. It is known that the converter can settle the 98% value of a power reference in 100 ms [1]. Considering the converter dynamics similar to a first order system, its time constant is four times the 98% time value, that is, $\tau = 25ms$. Considering

also and unitary gain, the transfer function G that approximates the performance of the converter is:

$$G = \frac{1}{25 \cdot 10^{-3}s + 1} \quad (5.6)$$

Figure 5.4 shows the Bode diagram of (5.6).

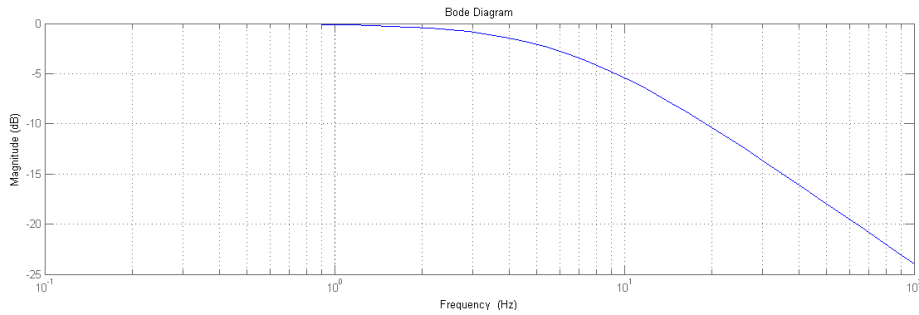


Figure 5.4: Converter Bode diagram

It can be seen that the higher the frequency is, the bigger is the attenuation. For a 10 Hz frequency there is a gain of -5 dB. Then, the power input will not importantly excite the oscillatory modes located at 10 Hz in the frequency domain seen in Figures 5.2 and 5.3.

Taking that into account, values for the K_{droop} a little bit higher than the one calculated in the previous chapter can also be valid, as for example, values compressed by $\frac{1}{45} < K_{droop} < \frac{1}{40}$. However, the valid values for K_{droop} compound a considerably tight range. For that reason, operating the DC grid implementing a droop control within this range, will not affect the system behaviour importantly.

The frequency analysis is useful to ensure that the operation of the converter will not exceed the defined limits even during transients.

Next, other cable models are analysed based on the same procedure.

5.4 Pi multi-section model analysis

Once the frequency behaviour of a single Pi section cable model has been analysed, in this section, an analogous study is carried out for the multiple Pi sections cable model.

5.4.1 Stability analysis

First of all, regarding the stability analysis it can be said that the system is stable for multiple sections. The stability tests are done but only a couple of cases are shown as example.

In Figure 5.6 the system is considerably complex, so much so that the number of poles is so high that they form a vertical straight line, although all of them have negative real part.

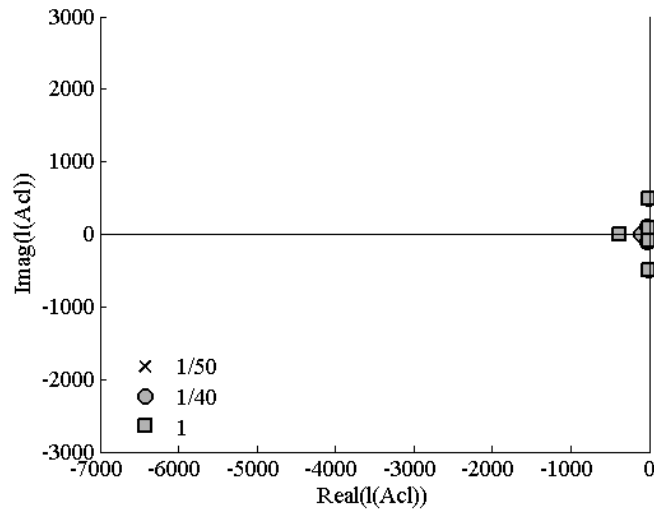


Figure 5.5: Stability analysis for 2 Pi sections

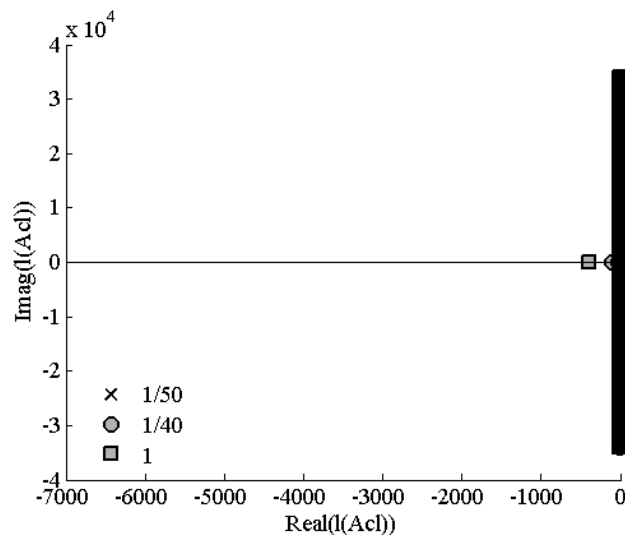


Figure 5.6: Stability analysis for 100 Pi sections

5.4.2 Frequency analysis

Once having seen that the system is stable no matter the number of sections, an analysis of the model behaviour is carried out based on the frequency response of $S(s)G_{yw}(s)$ and $KS(s)G_{yw}(s)$ starting for example, for two Pi sections.

It can be seen that the graphic is the same as the single section case, except for the peak that appear in 100 Hz frequency. The peak that appear at 10 Hz has almost the same shape. A more detailed observation shows that it is slightly shifted to the right side, but it only is appreciable if the two graphics are superposed. Furthermore, this fact does not change the previous conclusions, since the gain peaks around 10 Hz have a reduced effect in the response since the current input that comes from the wind farm side converter does

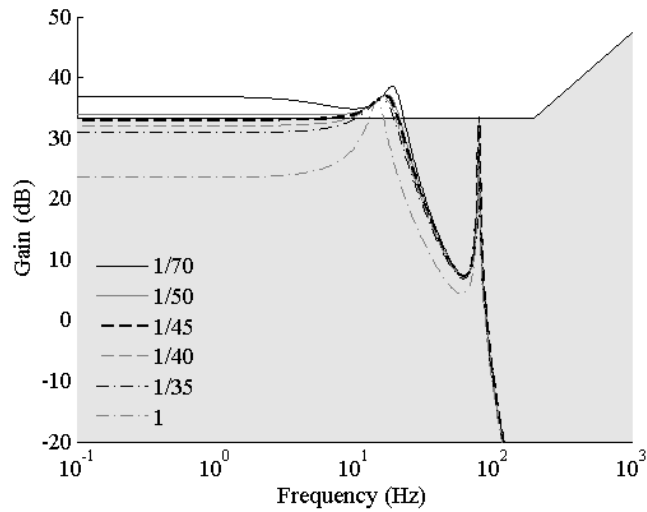


Figure 5.7: Bode diagram for $S(s)G_{yw}(s)$ (2 Pi sections)

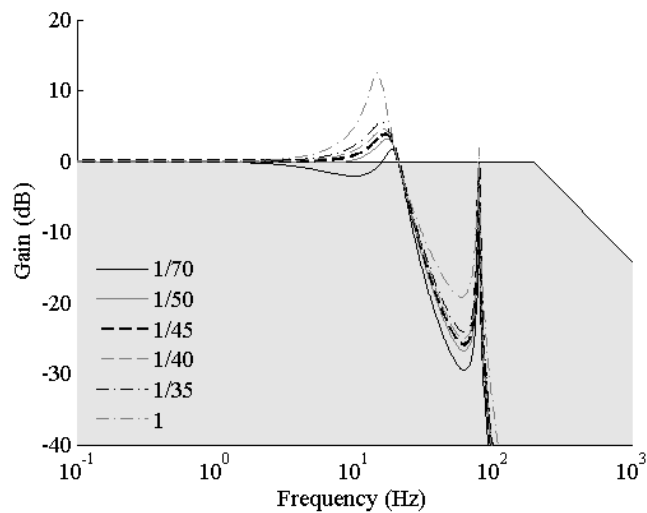


Figure 5.8: Bode diagram for $KS(s)G_{yw}(s)$ (2 Pi sections)

not excite those frequencies.

The same reasoning can be applied to the new peak that appear at 100 Hz. This frequency value is much bigger than the one before, so the effect that it might cause to the response is minor. Furthermore, its gain is lower than the peak of 10 Hz, this makes its effect even more insignificant.

Now lets see what happens if more than two sections are added. The same frequency analysis of $S(s)G_{yw}(s)$ and $KS(s)G_{yw}(s)$ is detailed for 10 and 50 Pi sections.

It can be seen that the higher is the number of Pi sections the higher is the number of peaks that appear. It can also be seen that these new peaks appear at high frequencies, more specifically, a new peak appears at a higher frequency than the peak before. The

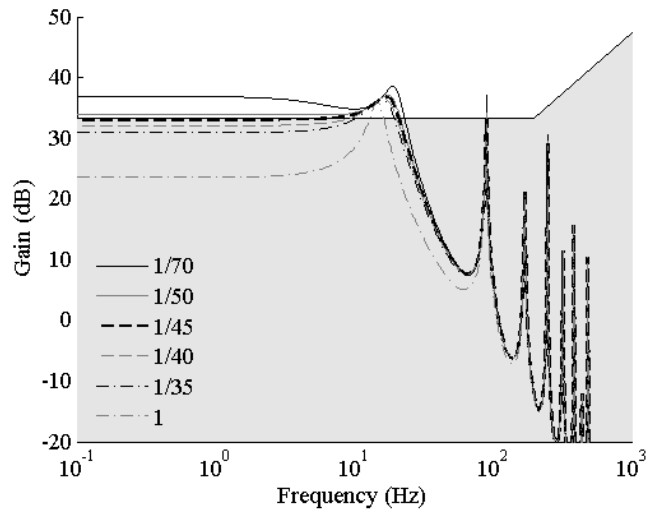


Figure 5.9: Bode diagram for $S(s)G_{yw}(s)$ (10 Pi sections)

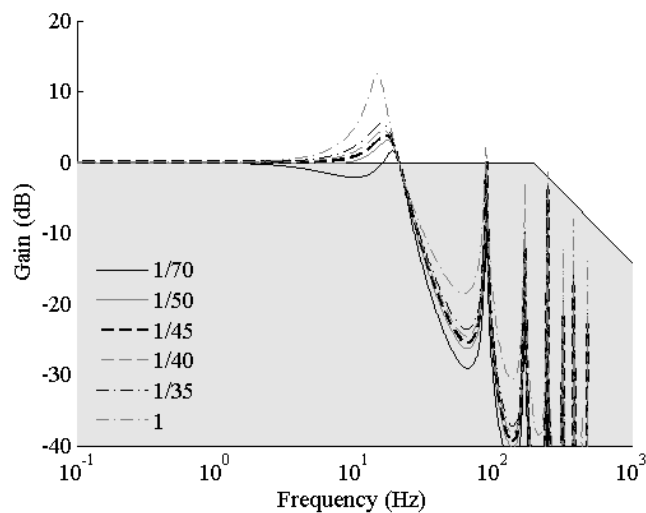


Figure 5.10: Bode diagram for $KS(s)G_{yw}(s)$ (10 Pi sections)

shape of the graphic under the 10 Hz frequency is quite similar no matter the number of Pi sections considered.

As said before, these peaks over the 10 Hz frequency does not have an important effect in the system response because the wind farm converter does not excite those modes in normal operation. For that reason, this study allows to conclude that for the Pi model the number of sections used for the K_{droop} calculation does not change the conclusions obtained with a simple Pi model.

However, as it is aforementioned, other models can be found in the literature. Next, the Pi coupled cable model is analysed.

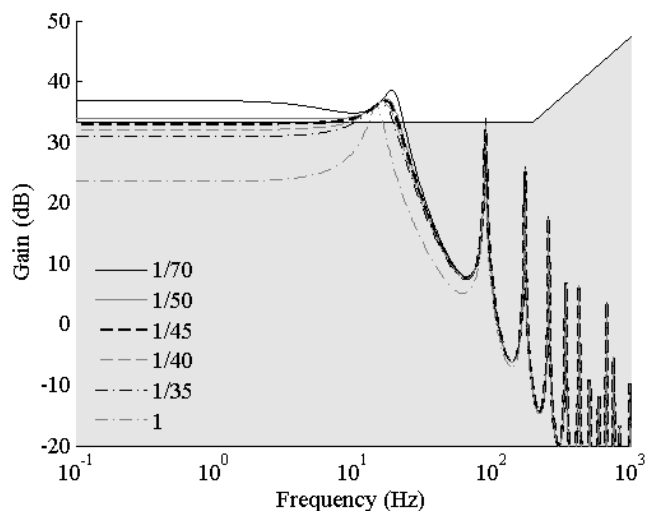


Figure 5.11: Bode diagram for $S(s)G_{yw}(s)$ (50 Pi sections)

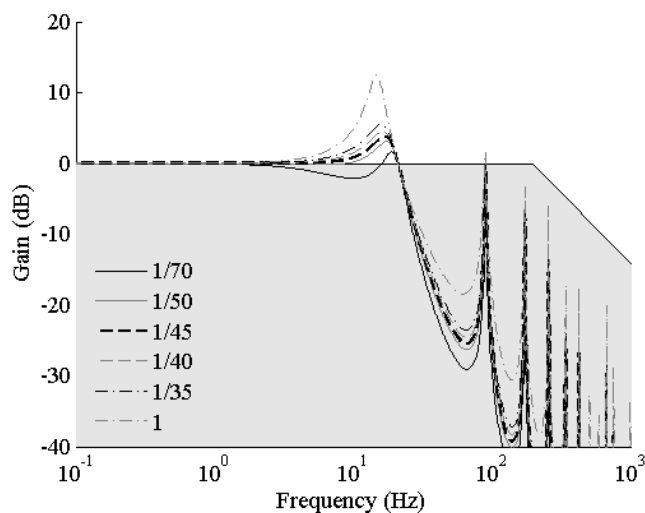


Figure 5.12: Bode diagram for $KS(s)G_{yw}(s)$ (50 Pi sections)

5.5 Pi coupled model analysis

As said in Chapter 3, the Pi model does not take into account the geometry of the cable. It might be important to consider the possible interaction between the cable core and the screen, this is the reason to analyse the Pi coupled model.

5.5.1 Stability analysis

The technique used to study the stability is equivalent to the one employed previously. Figure 5.13 shows the poles of the system when the Pi coupled model is included in the

analysis.

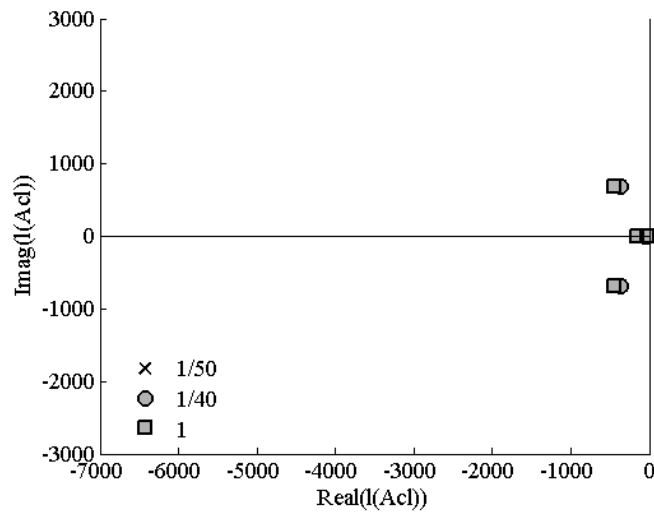


Figure 5.13: Stability analysis for Pi coupled model

As expected, it can be seen that it does not exist a pole with a positive real part, so the system is stable.

5.5.2 Frequency analysis

Again, the two Bode diagrams for $S(s)G_{yw}(s)$ and $KS(s)G_{yw}(s)$ are sketched below.

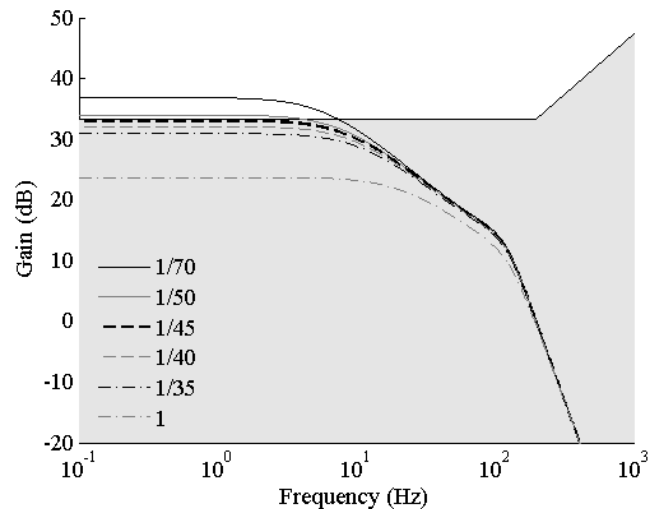


Figure 5.14: Bode diagram for $S(s)G_{yw}(s)$ (Pi coupled model)

As it can be seen, the frequency gain peaks found in previous sections are damped here. According to the Pi coupled model, the mutual inductance between the core cable and the screen, apparently mitigates any electrical resonance. Note that, according to this

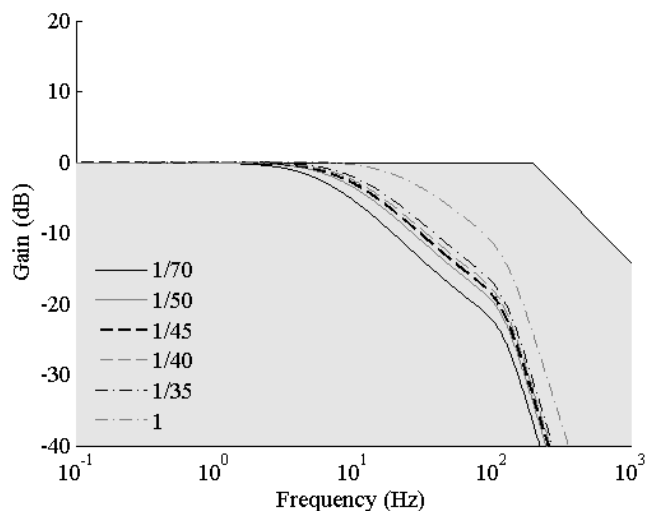


Figure 5.15: Bode diagram for $KS(s)G_{yw}(s)$ (Pi coupled model)

cable model, the K_{droop} value could be as large as the steady state maximum error and maximum current limits allow, because the largest gain peaks found in the Bode diagrams of $S(s)G_{yw}(s)$ and $KS(s)G_{yw}(s)$ are found at 0 Hz.

By using this model there is more flexibility in the K_{droop} design, but after all, it is worth to not forget that this is a model, it does not describe the reality perfectly, like any other model (including the Pi model).

Three different cable models have been used to design the droop control showing different results. The simple Pi and the Multiple-section Pi models show similar results, as the procedure of modelling is equivalent. However, the Pi coupled model shows an important difference compared to the other two, as it does not present important gain peaks at low frequencies.

For this reason, it is advisable to use the more conservative K_{droop} design in order to avoid problems during the operation. Then, the final value selected to operate the analysed grid is $\frac{1}{45}$.

Chapter 6

Simulation results

As it can be seen in the previous chapter, the K_{droop} value found when the steady state was considered, which was $\frac{1}{45}$, turned out to be valid for all frequencies. In this chapter, using that value, the implementation of this controller into the system will be studied and simulated using Matlab. The system parameters used during the simulations are sketched in table 5.1. Figure 6.1 shows the system implementation.

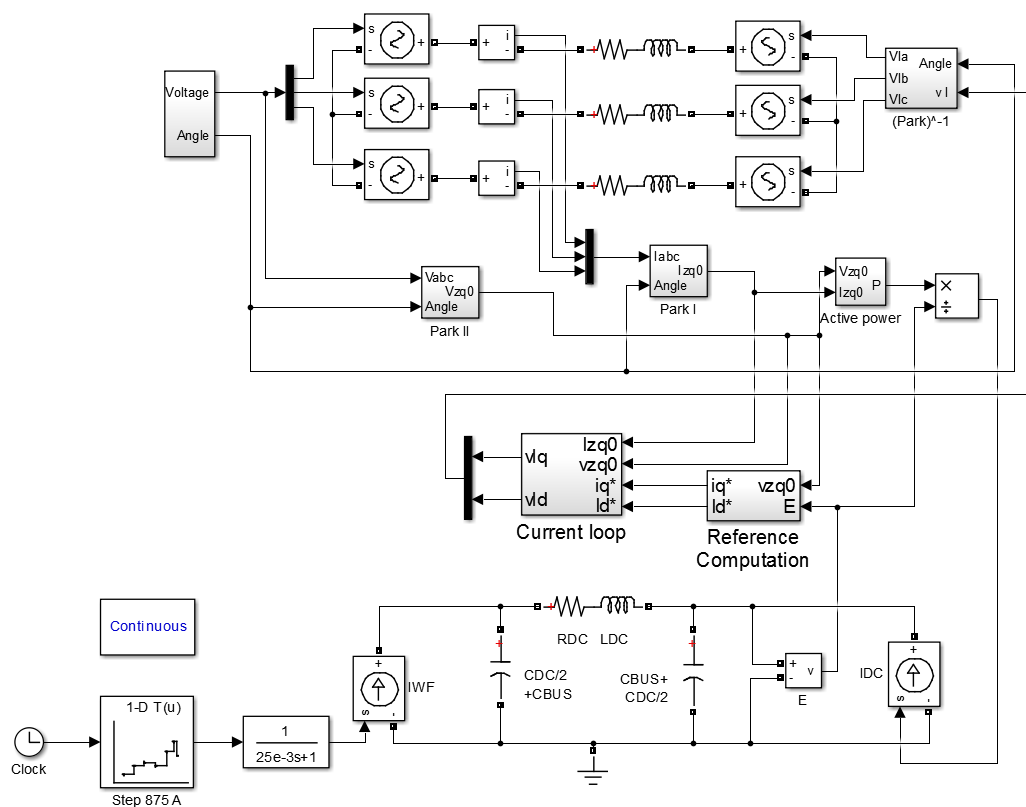


Figure 6.1: System implementation using Matlab Simulink

As it can be seen, all the elements detailed in Chapter 2 have been taken into account,

including the Reference computation detailed in Figure 6.2 and the Current loop sketched in Figure 6.3.

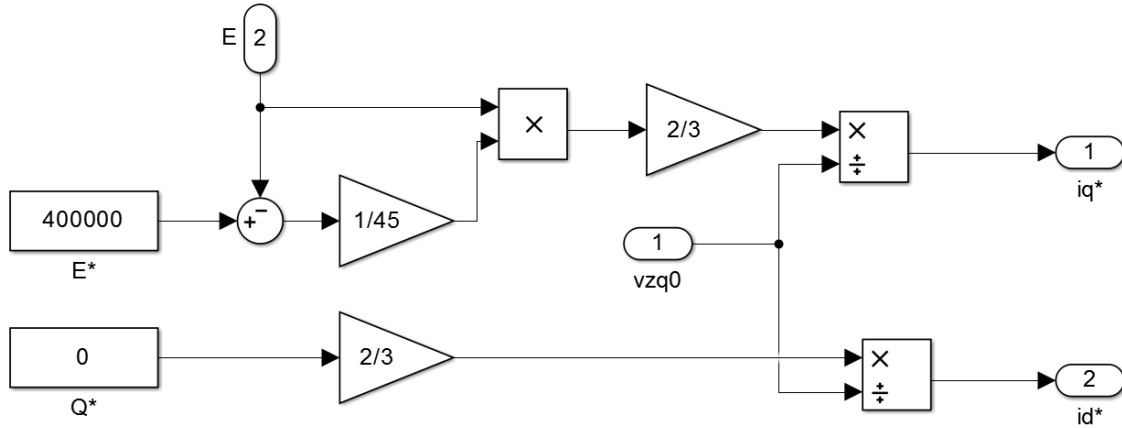


Figure 6.2: Droop control and reference computation implementation

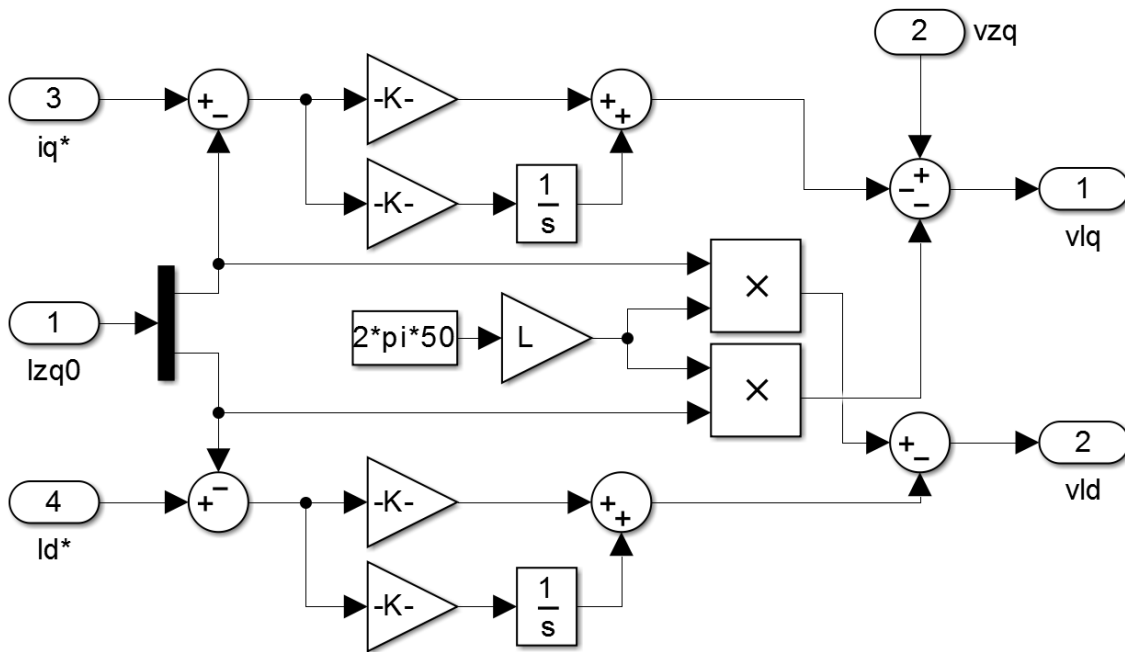


Figure 6.3: Current loop implementation

The calculation of the exchanged reactive power is achieved by using the power equations obtained when the Park transformation is applied, as it is explained in C. Its implementation in Matlab is detailed in the next Figure 6.4.

It is worth to remark that with this implementation the simplification for the current loop

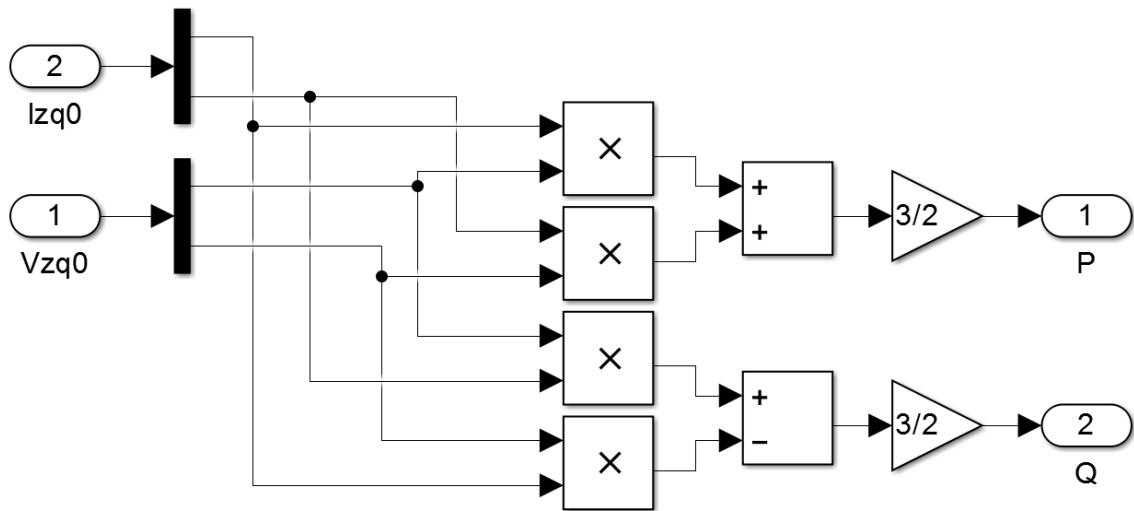


Figure 6.4: Reference computation implementation

done during the control design is not applied, for that reason, the simulation results are important in order to confirm that the so-mentioned simplification is valid.

The simulations to be shown are:

- DC voltage grid side converter response to a stepwise current input from the wind farm (I_{DC}).
- Grid side converter response to a current input from the wind farm considering the wind farm converter power loop.

In all the simulations showed in this chapter, it will be seen the temporal response in front a perturbation of 875 A, which is considered to be the rated current for the converter. Advancing results, it will be seen that the specified conditions during the K_{kdroop} design will be accomplished.

6.1 Temporal response of the DC droop controller in front of a stepwise current input

The next Figure 6.5 shows the temporal response of the DC bus for each studied model when, as said before, a current step with 875 A of amplitude is considered.

It can be seen that at steady state the error conditions are fulfilled (maximum error of 40 kV). However, it can be seen that this limit is exceeded transiently. This is because, as said in Chapter 5, the perturbation considered is a step, involving high frequency oscillations. This operation is not realistic, as the power loop of the wind farm converter is affecting the limiting the current variation speed.

In the next section, the dynamics of the power loop are included in the simulation.

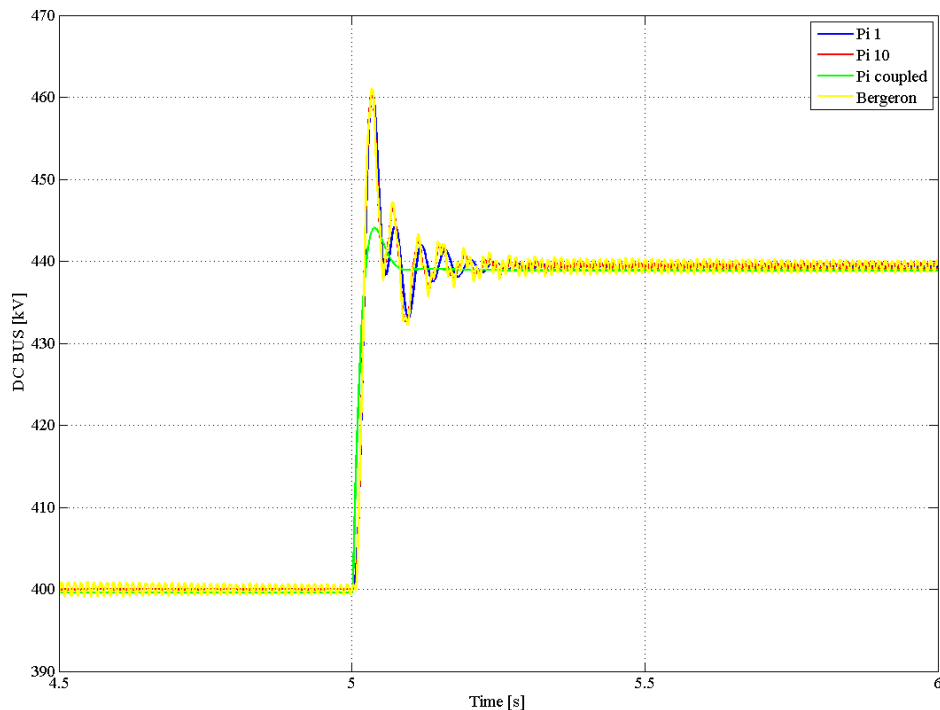


Figure 6.5: Temporal response of the DC bus for each model considering a 875 A step

6.2 Simulation results for a power step input

In this section, the current injected to the grid by the wind farm converter is modelled, as it is explained in Chapter 5 as a first order system with $25 \cdot 10^{-3}$ s of constant time.

Figure 6.6 and Figure 6.7 shows the temporal response of the DC currents and voltages comparing the response for the different cable models. The current from the wind farm is also plotted to compare it with the other DC currents.

It can be seen that the current response of all the models is quite similar to each other and, as expected, they are all similar to the external perturbation I_{DC} . Thus, as large peaks in the current are avoided, the droop design is validated.

Here the error specifications are almost perfectly fulfilled, so the K_{droop} design is considered to be valid.

Finally, to illustrate graphically the effect of the perturbation considering the abc frame, it is showed the AC grid current for each model when the perturbation is applied.

As expected, it can be seen that the differences between models are minimum.

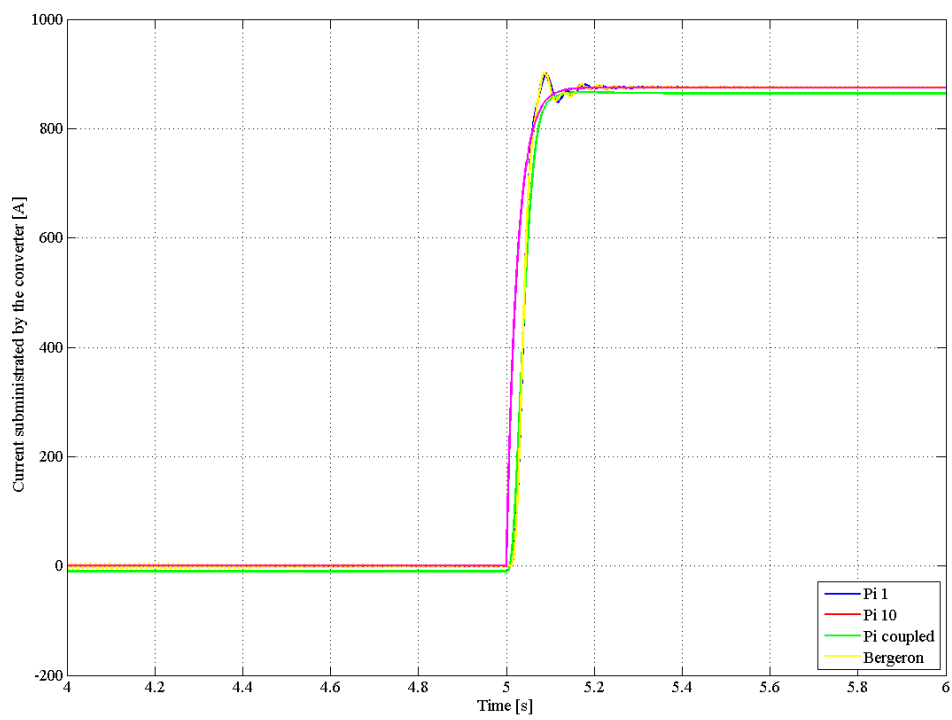


Figure 6.6: Temporal response of I_{DC} for the different cable models

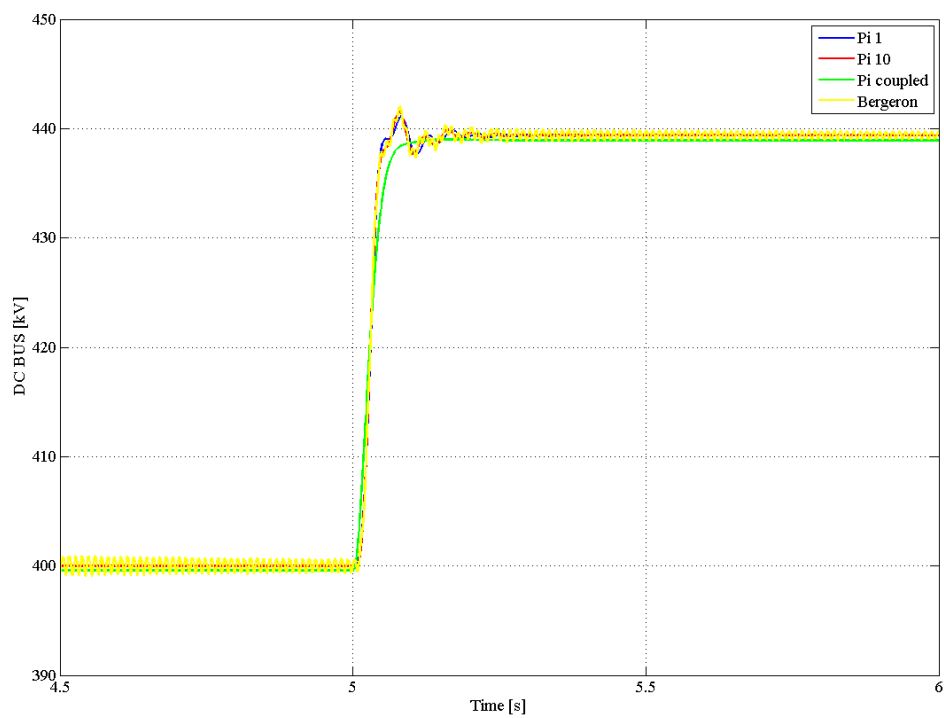


Figure 6.7: Temporal response of the DC bus for each model considering the wind farm converter

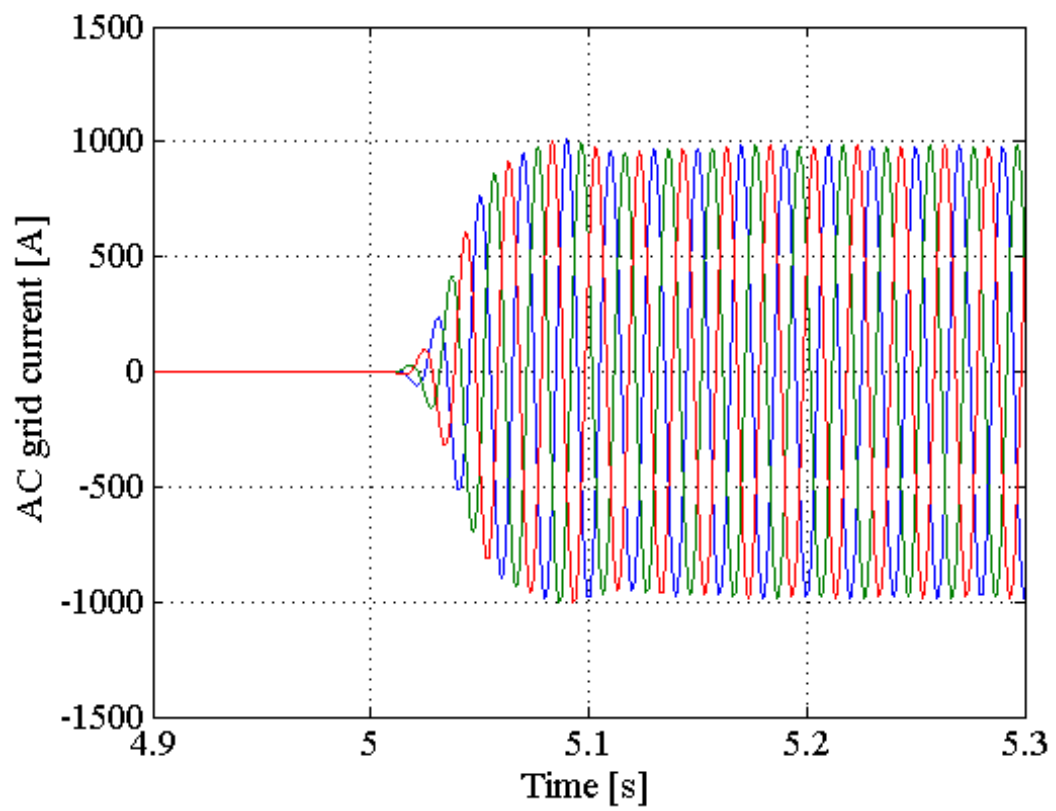


Figure 6.8: Temporal response of I_{abc} considering one Pi section

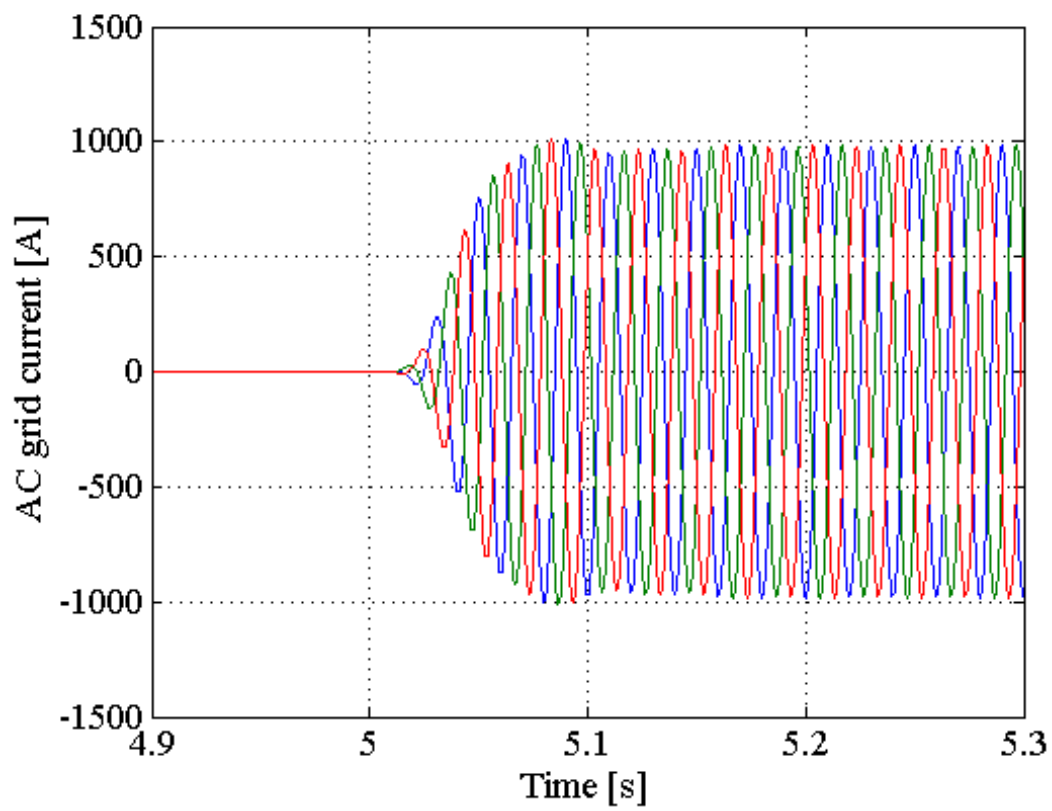


Figure 6.9: Temporal response of I_{abc} considering ten Pi sections

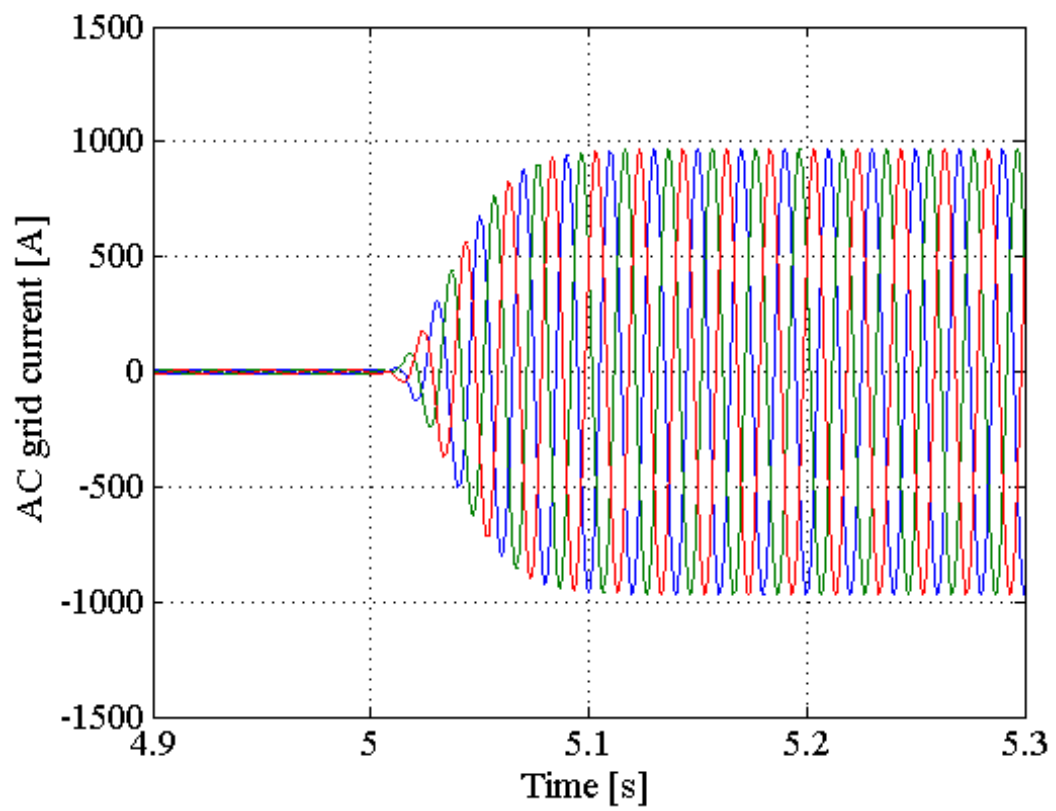


Figure 6.10: Temporal response of I_{abc} considering the Pi coupled model

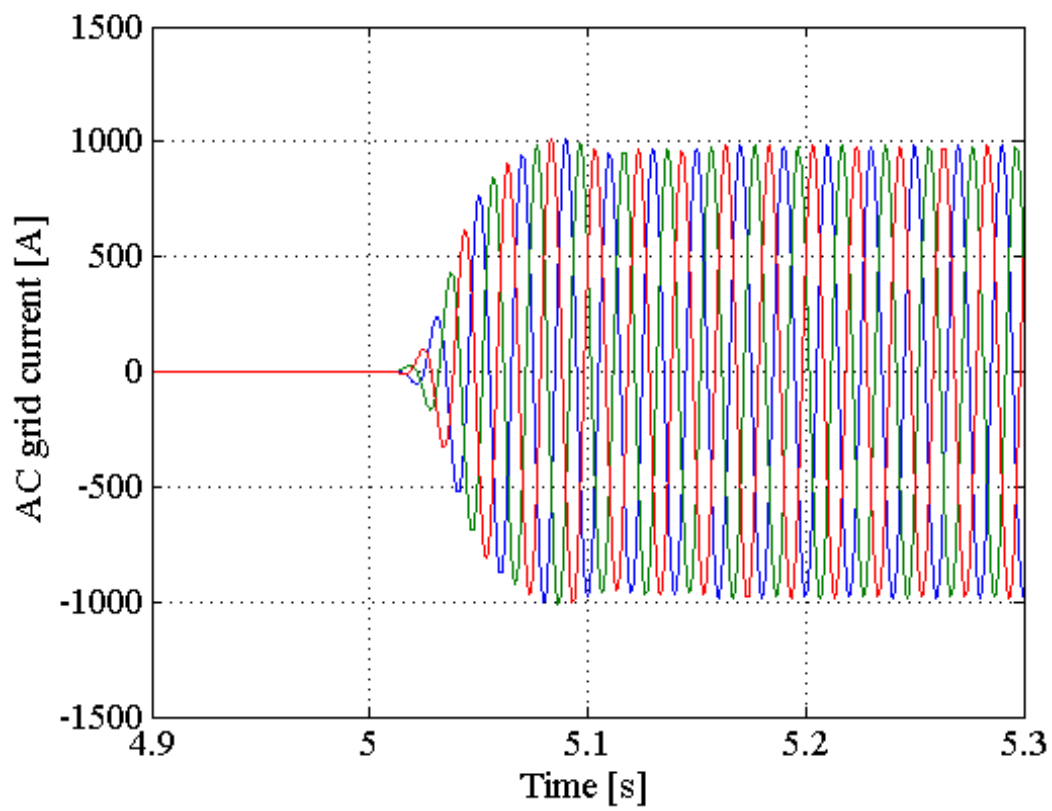


Figure 6.11: Temporal response of I_{abc} considering the Bergeron model

Conclusions

In this work it can be seen the system formed by the wind farm plant, the HVDC line that connects this plant to the AC grid line, and the VSC converter that makes possible this connection. The work is focussed in more detail in the VSC converter and the models used to describe the HVDC line.

One of the objectives of the work is to design of the DC bus voltage controller for the ground side converter. The proposed controller is a proportional droop controller and the design of its K_{droop} is discussed in this work from two points of view.

The first approach focusses on the steady state scenario in where by accepting a determinate error in front a certain perturbation, an initial value for the K_{droop} is found. In the second approach, the transient state is taken into account, for that reason the study focuses in all the frequency range. This second study allows to introduce a second condition for the K_{droop} design, that is, the limitation for the current injected by the converter in front an external perturbation, and with that, a range of valid values for K_{droop} is found. Moreover, although this is not the case of this work, it could be possible to find out that the K_{droop} value found with the first approach could not be valid when the transient state is considered. For that reason, it is worth to consider a frequency analysis in order to ensure the validity of the K_{droop} value.

It also can be seen that the HVDC model used could be a key point in the K_{droop} design. If the cable model is not accurate enough the K_{droop} design could be wrong. Due to this, it could be helpful to make the design using different models in aim to ensure the results.

Finally, a last remarkable conclusion found is that regarding the Pi model, if multiple sections are added its effect appears at high frequencies. Taking that into account, depending on the dynamics of the wind farm side converter, the effect of the multiple sections could have no significance into the obtained results, (which is the case in this work), and a single Pi section could be enough for modelling the HVDC line.

Acknowledgements

Per començar, m'agradaria donar les gràcies a tot el CITCEA per oferir-me la possibilitat de fer aquest projecte i per donar-me l'oportunitat de formar-me dins d'aquest àmbit de l'enginyeria el qual sempre m'ha atret. En especial, vull donar les gràcies a en Marc Llonch i a l'Enric Sánchez per la seva ajuda durant les etapes inicials, a l'Oriol Gomis per dirigir-me el projecte, i sobretot, a l'Eduardo Prieto que s'endú la major part del mèrit d'aquest projecte per tot el seu suport i dedicació constants.

A més a més, vull donar les gràcies a la meva família, no només per donar-me els mitjans materials que m'han fet falta, sinó també pels valors i l'educació que m'han inculcat i que m'han permès formar-me com a persona.

A tots ells, gràcies.

Annex A

Budget

The fact that this work does not include an experimental set-up makes the budget cheaper, because it will only include the necessary office supplies and the human resources. The estimated prices considered in the next sections do not include the taxes.

A.1 Office supplies

The office supplies are basically the computer used to do this work. In this section the cost of the computer and the software used is detailed in two subsections, hardware and software.

A.1.1 Hardware

Concept	Unitary price [€/u]	Units [u]	Price [€]
PC Samsung NP-R530	529,95	1	529,95
Total			529,95

Table A.1: Hardware

A.1.2 Software

The office supplies are useless without the appropriate software, which in this case, is Matlab Simulink and its price is detailed in the next table.

Concept	Unitary price [€/u]	Units [u]	Price [€]
Matlab [®] with SimPowerSystems libraries	2.100	1	2.100
Latex editor	0	1	0
Total			2.100

Table A.2: Software

A.2 Human resources

In this part of the work the activities are divided in three blocks which are training and research, simulation, and drafting. The price of each part is detailed in the next table.

Concept	Price per hour [€/h]	Hours [h]	Price [€]
Training and research	35	220	7.700
Simulation	35	160	5.600
Drafting	20	70	1.400
Total			14.700

Table A.3: Human resources

A.3 Total budget

By adding the cost of the two previous sections the total cost of the project is obtained.

Concept	Price [€]
Hardware	529,95
Software	2.100
Human resources	14.700
Total	17.329,95

Table A.4: Total budget

Annex B

Environmental impact assessment

A wind farm can cause many impacts in the environment and this can be different in each state of its lifetime (installation, operating state and dismantling). There are two principal components that cause impact, the wind turbines itself and the HVDC line. The impact of the wind turbines are similar to the onshore ones, but adding the impact that they might cause into the seabed and the marine ecosystem. For the cables, its impact is the same as the HVAC cables during the construction phase, and its main affectation is due that they are installed in the seabed. In this section the main impacts will be discussed and classified depending on the type impact.

B.1 Seabed impact

This is the more obvious impact. In order to hold the wind turbines a structure needs to be cemented into the seabed. This requires a previous study to find the better location to cement in. This study has to take into account the soil composition in order to ensure the minimum impact, the maximum reliability and the minimum operation cost if it is possible. In relation to the HVDC line, the measures are similar. It does not require the seabed to be cemented but it is necessary to take into account the line trajectory to minimize the environment impact. For example the location of coral colonies has to be taken into account if they are near to the line trajectory, or other possible factors that depend of the location of the line, such for example archaeological remains.

B.2 Marine ecosystem impact

This is closely related with the impact in the seabed. To begin with, the structure that supports the wind farm clearly will modify the habitat of the animals in the zone. This will be more notorious during the building process but once finished this stage this structure will form part of the habitat. The more obvious problem in a long term point of view will be the constant noise that the wind farm will produce during its performance. Related to the cable, the most notorious effect will be during its installation in the seabed because the

flora and fauna present along the line trajectory will be directly affected. The procedure to install the HVDC line is showed in B.1.

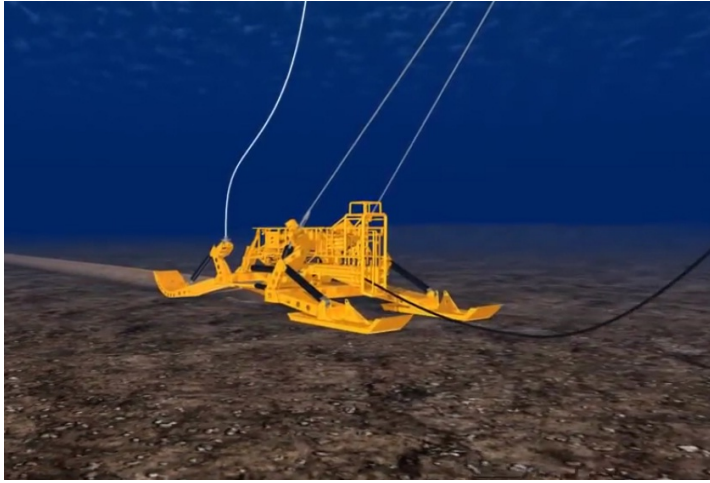


Figure B.1: HVDC installation

The procedure is done with a machine that opens the seabed, introduces the HVDC cable and finally re-closes the gap at the same time. The machine is conducted by a water-craft that is also responsible of providing the cable that will be installed (the black wire in B.1). A consequence of this operation is the apparition of suspended solids due to the soil movement. All the effects that this will cause to the ecosystem has to be studied in order to minimize the environment degradation.

B.3 Atmospheric effects

The only negative effect that a wind farm might cause to the atmosphere is that depending on its location it might alter the migration of local birds. In that aspect the impact is similar to an onshore wind farm and a study to minimize this consequence has to be taken into account. For the other hand, a wind farm has a positive effect on the atmosphere because it allows to obtain energy without generating CO_2 emissions.

B.4 Impact in humans

In contrast to other energy sources, the wind farm generation does not have any potential dangers for the human security. The only affectations that it might cause were in navigation and fishing. For this reason a factor to take into account to decide the location of the wind farm is if it would affect shipping routes. Another factor that a wind farm might cause is the visual impact depending of the distance of its location to the coast.

Annex C

Park transformation

The Park transformation allows to obtain constant quantities from magnitudes of oscillating nature [2]. This is specially useful in the control design of a three-phase balanced system and it is used along this work. A three-phase balanced system consists in 3 electrical phasors separated by 120 degrees. This three phasors rotate at speed $\dot{\theta} = 2\pi f$ where θ is the electrical grid angle which changes along the time with the frequency grid. Once having seen this, the first step for representing the information contained in these phasors in constant quantities is applying the Clarke transformation as the next definition denotes.

$$\begin{bmatrix} X_\alpha \\ X_\beta \\ X_0 \end{bmatrix} = \frac{2}{3} \begin{bmatrix} 1 & -\frac{1}{2} & -\frac{1}{2} \\ 0 & -\frac{\sqrt{3}}{2} & \frac{\sqrt{3}}{2} \\ \frac{1}{2} & \frac{1}{2} & \frac{1}{2} \end{bmatrix} \begin{bmatrix} X_a \\ X_b \\ X_c \end{bmatrix} \quad (\text{C.1})$$

This transformation changes the reference from the abc phasors to a $\alpha\beta 0$ frame. The next example will help to understand geometrically this transformation. Let's imagine that the abc phasors are the red edges of the cube of the figure C.1.

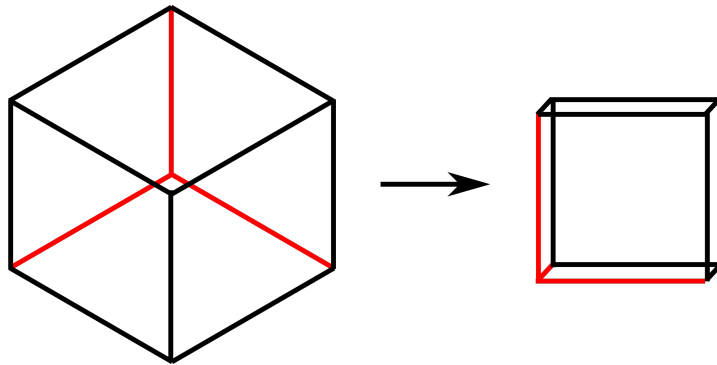


Figure C.1: Geometrical interpretation

It can be seen that the result of this transformation is two perpendicular phasors contained in the $\alpha\beta 0$ frame and another one perpendicular to that frame which its value is zero. This is useful because now the information is contained in two phasors instead of three, but these two phasors are still spinning with the grid angle θ . This problem is overcome by using

a coordinate system that spins in conjunction with the grid. To do this rotation the grid angle has to be known, and as explained in this work, this is achieved thanks to the PLL. The rotation is done by using the next transformation.

$$\begin{bmatrix} X_q \\ X_d \\ X_0 \end{bmatrix} = \begin{bmatrix} \cos\theta & \sin\theta & 0 \\ -\sin\theta & \cos\theta & 0 \\ 0 & 0 & 1 \end{bmatrix} \begin{bmatrix} X_\alpha \\ X_\beta \\ X_0 \end{bmatrix} \quad (\text{C.2})$$

By combining the Clarke transformation plus the appropriate rotation the so called Park transformation is obtained.

$$\begin{bmatrix} X_q \\ X_d \\ X_0 \end{bmatrix} = \frac{2}{3} \begin{bmatrix} \cos\theta & \sin\theta & 0 \\ -\sin\theta & \cos\theta & 0 \\ 0 & 0 & 1 \end{bmatrix} \begin{bmatrix} 1 & -\frac{1}{2} & -\frac{1}{2} \\ 0 & -\frac{\sqrt{3}}{2} & \frac{\sqrt{3}}{2} \\ \frac{1}{2} & \frac{1}{2} & \frac{1}{2} \end{bmatrix} \begin{bmatrix} X_a \\ X_b \\ X_c \end{bmatrix} = \frac{2}{3} \begin{bmatrix} \cos\theta & \cos(\theta - \frac{2\pi}{3}) & \cos(\theta + \frac{2\pi}{3}) \\ \sin\theta & \sin(\theta - \frac{2\pi}{3}) & \sin(\theta + \frac{2\pi}{3}) \\ \frac{1}{2} & \frac{1}{2} & \frac{1}{2} \end{bmatrix} \begin{bmatrix} X_a \\ X_b \\ X_c \end{bmatrix} \quad (\text{C.3})$$

The Park transformation is not unique. There are other types of transformations in which varies the way in which the first change of reference is done, but the idea behind this is the same. The Park transformation showed above is the one used in this work, and has the property to maintain constant the amplitude of the phasors. With that, the calculation of the active and reactive power results.

$$P = \frac{3}{2}(v_q i_q + v_d i_d) \quad (\text{C.4})$$

$$Q = \frac{3}{2}(v_q i_d + v_d i_q) \quad (\text{C.5})$$

Annex D

Distributed parameters model vs Bergeron line model

The Distributed Parameters model consists in solving the system of equations that are written in a differential of cable. The process is similar at the Bergeron model at the beginning, but the final results are apparently different. The derivation of this model will be explained below. After deducing its final equations, it will be demonstrated that this two models are the same. As is shown in the next Figure, a differential of line is taken. This time the resistance is taken into account

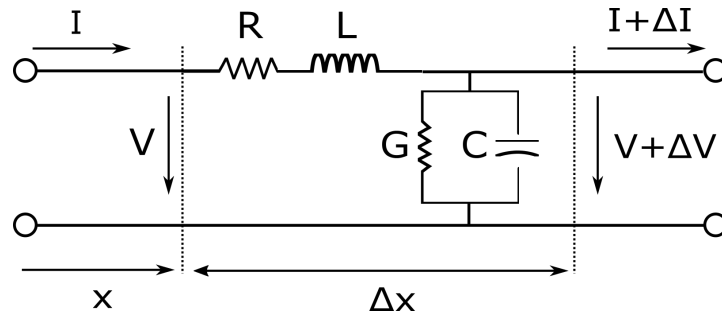


Figure D.1: Differential of cable

$$\Delta V = \frac{dV}{dx} \cdot \Delta x = -(R \cdot \Delta x) \cdot I - (L \cdot \Delta x) \cdot \frac{dI}{dt} \quad (\text{D.1})$$

$$\Delta I = \frac{dI}{dx} \cdot \Delta x = -(G \cdot \Delta x) \cdot V - (C \cdot \Delta x) \cdot \frac{dV}{dt} \quad (\text{D.2})$$

Being R , L , G and C the electric parameters per unit length. Simplifying Δx at each side of the equations and transforming it into Laplace domain the next system is obtained.

$$\frac{dV(x, s)}{dx} = -(R + Ls) \cdot I(x, s) \quad (\text{D.3})$$

$$\frac{dI(x, s)}{dx} = -(G + Cs) \cdot V(x, s) \quad (\text{D.4})$$

Applying the derivative of the two equations respect to x the system has the form:

$$\frac{d^2V(x, s)}{dx^2} = (R + Ls) \cdot (G + Cs) \cdot V(x, s) \quad (\text{D.5})$$

$$\frac{d^2I(x, s)}{dx^2} = (R + Ls) \cdot (G + Cs) \cdot I(x, s) \quad (\text{D.6})$$

It can be seen that in this notation $V(x, s)$ and $I(x, s)$ are multiplied by a function that only depends of s . That allows to obtain a general solution for this type of differential equation which has the form:

$$V(x, s) = V_1(s)e^{\beta x} + V_2(s)e^{-\beta x} \quad (\text{D.7})$$

$$I(x, s) = \frac{V_1(s)e^{\beta x} - V_2(s)e^{-\beta x}}{Z_c(s)} \quad (\text{D.8})$$

Where the functions $\beta(s)$ and $Z_c(s)$ are:

$$\beta(s) = \sqrt{(R + Ls) \cdot (G + Cs)} \quad (\text{D.9})$$

$$Z_c(s) = \sqrt{\frac{(R + Ls)}{(G + Cs)}} \quad (\text{D.10})$$

V_1 and V_2 are functions that depend of s and for find its expression is necessary to determinate the boundary conditions. Taking the electrical values in the beginning of the line as V_r and I_r , a relation between V_1 and V_2 can be obtained as the next expressions show.

$$V_r = V(0, s) = V_1(s)e^{\beta \cdot 0} + V_2(s)e^{-\beta \cdot 0} = V_1 + V_2 \quad (\text{D.11})$$

$$I_r = I(0, s) = \frac{V_1(s)e^{\beta \cdot 0} - V_2(s)e^{-\beta \cdot 0}}{Z_c(s)} = \frac{V_1 - V_2}{Z_c} \quad (\text{D.12})$$

This allows to obtain an expression of V_1 and V_2 in function of the electrical state of the beginning of the line.

$$V_1 = \frac{V_r + I_r Z_c(s)}{2} \quad (\text{D.13})$$

$$V_2 = \frac{V_r - I_r Z_c(s)}{2} \quad (\text{D.14})$$

By substituting V_1 and V_2 in (D.7), the general expressions of the parameter transmission line are obtained.

$$V(x, s) = \left(\frac{V_r + I_r Z_c(s)}{2} \right) e^{\beta x} + \left(\frac{V_r - I_r Z_c(s)}{2} \right) e^{-\beta x} \quad (\text{D.15})$$

$$I(x, s) = \left(\frac{V_r + I_r Z_c(s)}{2Z_c(s)} \right) e^{\beta x} - \left(\frac{V_r - I_r Z_c(s)}{2Z_c(s)} \right) e^{-\beta x} \quad (\text{D.16})$$

Rearranging the above expressions, the next form can be obtained.

$$V(x, s) = \left(\frac{e^{\beta x} + e^{-\beta x}}{2} \right) V_r + Z_c(s) \left(\frac{e^{\beta x} - e^{-\beta x}}{2} \right) I_r \quad (\text{D.17})$$

$$I(x, s) = \frac{1}{Z_c(s)} \left(\frac{e^{\beta x} - e^{-\beta x}}{2} \right) V_r - \left(\frac{e^{\beta x} + e^{-\beta x}}{2} \right) I_r \quad (\text{D.18})$$

Note that the exponential forms of the hyperbolic functions $\sinh(x)$ and $\cosh(x)$ appear in the above expressions. Taking that into account, the final form of the parameter transmission line can be obtained and can be written in a matrix notation.

$$\begin{bmatrix} V_s \\ I_s \end{bmatrix} = \begin{bmatrix} \cosh(\beta l) & Z_c(s) \sinh(\beta l) \\ \frac{1}{Z_c(s)} \sinh(\beta l) & \cosh(\beta l) \end{bmatrix} \begin{bmatrix} V_r \\ I_r \end{bmatrix} \quad (\text{D.19})$$

Once having seen this, it will be demonstrated that this model is just the same as the Bergeron line model. Transforming the Bergeron equations into Laplace domain it can be seen that:

$$I_r = \frac{V_r}{Z_c} - \frac{V_s}{Z_c} e^{-\beta l} - I_s e^{-\beta l} \quad (\text{D.20})$$

$$I_s = \frac{V_s}{Z_c} - \frac{V_r}{Z_c} e^{-\beta l} - I_r e^{-\beta l} \quad (\text{D.21})$$

From the second equation the expression of V_s can be obtained and from the first one I_s is obtained.

$$V_s = I_s Z_c + V_r e^{-\beta l} + I_s e^{-\beta l} Z_c \quad (\text{D.22})$$

$$I_s = -\frac{V_s}{Z_c} + \frac{V_r}{Z_c} e^{\beta l} - I_r e^{\beta l} \quad (\text{D.23})$$

Substituting (D.22) into (D.23) and rearranging the resulting expression:

$$V_s = V_r \left(\frac{e^{\beta l} + e^{-\beta l}}{2} \right) + I_r Z_c \left(\frac{e^{-\beta l} - e^{\beta l}}{2} \right) \quad (\text{D.24})$$

In a similar way, by substituting (D.23) into (D.22) and rearranging the expression:

$$I_s = \frac{V_r}{Z_c} \left(\frac{e^{\beta l} - e^{-\beta l}}{2} \right) - I_r \left(\frac{e^{-\beta l} + e^{\beta l}}{2} \right) \quad (\text{D.25})$$

Taking into account the hyperbolic expressions from \cosh and \sinh

$$\cosh x = \frac{e^x + e^{-x}}{2} \quad (\text{D.26})$$

$$\sinh x = \frac{e^x - e^{-x}}{2} \quad (\text{D.27})$$

It can be seen that equations (D.24) and (D.25) are the same as the above mentioned (D.19).

Bibliography

- [1] Til Kristian Vrana, Yongatao Yang, Sebastien Dennerrière, Jose Jardini, and Hani Saad. The CIGRE B4 DC Grid Test System. Technical report, 2013. [16](#), [41](#), [45](#)
- [2] Agustí Egea-Alvarez, Adria Junyent-Ferré, and Oriol Gomis-Bellmunt. Active and reactive power control of grid connected distributed generation systems. In *Modeling and Control of Sustainable Power Systems*, pages 47–81. Springer, 2012. [17](#), [19](#), [71](#)
- [3] Marc Cheah Mañé. *Implementació d'una microxarxa monofàsica basada en convertidors de tipologia VSC*. PhD thesis, Universitat Politècnica de Catalunya. [19](#)
- [4] Se-Kyo Chung. A phase tracking system for three phase utility interface inverters. *Power Electronics, IEEE Transactions on*, 15(3):431–438, 2000. [22](#)
- [5] Eduardo Prieto Araujo. Anàlisi dinàmica de xarxes multiterminal HVDC-VSC per al transport d'energia elèctrica en corrent continu en parcs eòlics marins. 2011. [11](#), [15](#), [16](#), [25](#), [41](#)
- [6] Antony James Beddard. Factors Affecting the Reliability of VSC-HVDC for the Connection of Offshore Windfarms. 2014. [28](#)
- [7] Rault Pierre. *Dynamic Modeling and Control of Multi-Terminal HVDC Grids*. PhD thesis, 2014. [28](#), [41](#)
- [8] Jr John J. Grainger, William D. Stevenson. *Análisis de sistemas de potencia*. McGraw-Hill, México, 1996. [30](#)
- [9] H.W. Dommel. Digital Computer Solution of Electromagnetic Transients in Single- and Multiphase Networks. *IEEE Transactions on Power Apparatus and Systems*, PAS-88(4):388–399, 1969. [30](#)
- [10] Eduardo Prieto-Araujo, Fernando D Bianchi, Adrià Junyent-Ferre, and Oriol Gomis-Bellmunt. Methodology for droop control dynamic analysis of multiterminal vsc-hvdc grids for offshore wind farms. *Power Delivery, IEEE Transactions on*, 26(4), 2011. [35](#), [37](#), [38](#), [43](#)
- [11] Sigurd Skogestad and Ian Postlethwaite. *Multivariable feedback control: analysis and design*, volume 2. Wiley New York, 2007. [37](#), [43](#)
- [12] Ricard Villà. *Dinàmica de Sistemes*. [37](#), [43](#)